Protein Integrated Light-Emitting Diodes

by

Rustamzhon Melikov

A Thesis Submitted to the

Graduate School of Sciences and Engineering

in Partial Fulfillment of the Requirements for

the Degree of

Master of Science

in

Electrical and Electronics Engineering

Koc University

September 2016

Koc University

Graduate School of Sciences and Engineering

This is to certify that I have examined this copy of a master's thesis by

Rustamzhon Melikov

and have found that it is complete and satisfactory in all respects,
and that any and all revisions required by the final
examining committee have been made.

Committee Members:

_____

Assist. Prof Sedat Nizamoğlu (advisor)

_____

Assist. Prof Şükrü Ekin Kocabaş

_____

Assoc. Prof. Ahmet Levent Subaşı

_____

Date: _____

To Abdurahmon MELIKOV …

ABSTRACT

The invention of efficient blue light-emitting diodes (LEDs) opened up a way toward bright and energy-saving white light sources which have a significant potential to replace conventional light sources. Solid state lighting (SSL) has so far been based on artificial or engineered wavelength-converter materials such as phosphors, synthetic dyes and inorganic nanocrystals without considering their environmental effects (e.g., toxicity). The expected high future-demand for SSL will lead to the generation of massive amount of electronic waste (e-waste). The integration of green materials into SSL can enhance environmental protection and sustainability. For this purpose, we integrated fluorescent and transparent proteins on light-emitting optoelectronic device structures to demonstrate eco-friendly LEDs. In this study, we used fluorescent proteins as color conversion materials and we introduced silk fibroin hydrogel as a lens material for light emitting diodes. The combinations of different protein emitters enable sensitive tuning of photometric quantities for application-specific lighting sources. To understand the technological limits of fluorescent protein integrated white LEDs, we simulated numerically white light generation using combinations of fluorescent proteins to calculate the maximum-attainable color rendering index and luminous efficacy of radiation. We experimentally optimized the expression and purification levels of fluorescent proteins that allow for chip-scale integration of proteins and white light generation. We demonstrated warm, daylight and cool white LEDs using biologically-derived fluorescent proteins for general lighting. These biomaterial-based LEDs exhibited color-rendering indices of up to 83, which is higher than conventional white LEDs made of yellow phosphor (around 68), and luminous efficiencies of up to 6.7 lm/W. Furthermore, we exhibited their use in liquid-crystal television (TV) for the first time.

In addition, we explored silk fibroin as a bio-friendly alternative to conventional polymers for lens application in light emitting diodes. We systematically investigated the properties of the silk hydrogels including transmittance and light extraction efficiency at

various concentrations for LED lenses. We demonstrated a high-control on the intensity distribution of spatial radiation via dome- and crater-shaped hydrogel lens structures. Hydrogel lenses with a silk fibroin concentration of 3.0 wt% showed the maximum light extraction efficiency of 94%. The experimental results of spatial radiation were complimented with the theoretical modelling of silk hydrogel lenses. The results based on eco-friendly fluorescent and silk proteins point toward a new direction in solid-state lighting.

ÖZET

Verimli mavi ışık yayan diyotların icadı, parlak ve enerji tasarruflu beyaz ışık kaynaklarına yol açtı, böylece geleneksel ışık kaynaklarıyla değişilebilecek potansiyele sahip olurlar. Katı hal aydınlatma için beklenen yüksek talep, büyük elektronik atik miktarina yol açacaktır. Katı-hal aydınlatma şimdiye kadar yapay veya mühendislik dalgaboyu-dönüştürücü malzemeleri olan fosfor, sentetik boyalar ve inorganik nanokristalleri kullanmaktadır, ama bu malzemeler toksik ve nadir toprak malzemelerini kullanir. Böylece, yeşil malzemelerin elektronik içine entegrasyonu, çevre koruma ve sürdürülebilirlik için daha önemli hale gelmektedir. Burada, ilk kez LEDlere proteinlerin bütünleşmesini sunuyoruz. Bu çalışmada, mavi LED'lerin elektrolüminesanı ve floresan proteinlerin fotolüminesansı kullanılarak renk dönüşümü gösterilmektedir ve ipek hidrojel malzemesi ışık yayan diyotlar (LED'ler) için bir lens materyali olarak tanıtılmıştır. Mümkün olabilecek maksimum renk aygılama indeksi ve diğer optik parametreleri hesaplamak için 12 floresan proteini kullanarak beyaz ışık üretimini simüle ettik. Deneysel şekilde biyolojik kaynaklı floresan proteinler kullanılarak elde edilen sıcak, gün ışığı ve soğuk beyaz LED'ler sıvı kristal ekranlarda ve genel aydınlatmalarda kullandık. Optimize edilmiş ve üretilmiş floresan proteinlerinin çip ölçekli entegrasyonuna ve beyaz ışık üretimine olanak sağladığını gösterdik. Sarı fosfordan yapılmış geleneksel beyaz LEDlerden daha yüksek CRI değeri (68) olan bu biyomalzeme tabanlı LED'le 83e kadar CRI ve en fazla 6.7 lm / W ışık verimliliği sergilemiştir. Farklı protein yayıcıların kombinasyonları uygulamaya özel ışık kaynakları için hassas fotometrik değerlerin avantajlı şekilde kullanılmasına olanak sağlamıştır. Daha sonra, sistematik şekilde çeşitli konsantrasyonlarda olan ipek hidrojel lenslerin özellikleri olan geçirgenliğini ve ışık çıkarma verimliliğini inceledik. Kubbe ve krater şeklindeki hidrojel lens yapılarının üzerindeki yüksek kontrollu mekansal radyasyon yoğunluğunun dağılımını gösterdik. Mekansal radyasyon deneysel sonuçları teorik modellenmiş ipek hidrojel lensler ile tamamlanılmıştır. Ayrıca, 3.0 % ağırlıklı bir ipek konsantrasyonda hidrojel lensler, 94 % ışık çıkarma verimliliğini göstermektedir. İpek hidrojel, ışık yayan

diyotlar için alternatif bir çevre dostu lens materyali olarak gösterilebilir. Bu çalışmada proteinlere dayalı katı hal aydınlatmalarda yeni yol açıldığını gözlemleyebiliriz.

ACKNOWLEDGEMENTS

I am grateful to my advisors, Assist. Prof. Sedat Nizamoğlu and Dr. Daniel Aaron Press for their guidance and contribution to my studies. I want to thank jury committee members Assist. Prof. Şükrü Ekin Kocabaş and Assoc. Prof. Ahmet Levent Subaşı for their feedback. Being a member of IDEALAB was a pleasure for me. I also would like to thank Dr. Ganesh Kumar Baskaran, Dr. Mariana Chirea, Dr. Elif Nur Fırat Karalar for their valuable time and comments.

I acknowledge the financial support of the Scientific and Technological Research Council of Turkey (TÜBİTAK) (114E194) , (114F317) and Marie Curie Career Integration Grant (PROTEINLED, 631679) during my M.Sc. study. Additionally, I am grateful for the facilities that Koç University provided.

Special thanks to Anıl Fettahoğlu, Itır Bakış Doğru, Sadra Sadeghi, Houman Bahmani Jalali, Mohamad Mohamadi Aria, Deniz Conkar, Reza Rahighi and Cemal Yamak for their contribution to my studies.

I am also grateful to my other officemates Bilgesu Erdoğan, Efe Elbeyli, Özgun Can Önder, Aysima Hacısuleyman, Serena Muratcioğlu, Maryam Dabaghchian, Sıla Özdemir, Yusuf Doğuş Doğru, Suha Mutluergil, Erkut Demirhan, Burcu Kulahçioğlu, Hassam Salehe Matar and Saeedah Mokarian for all the time we spent together at Koç University.

Finally, I want to thank my family for their support, encouragement and love.

Contents

List of figures

List of tables

Chapter 1 Introduction

Today conventional light sources consume about 20% of global electricity production and solid state lighting (SSL) offers 50% reduction in electricity consumption and reduces 28 million tons of carbon emission per year [1]. SSL has gained significant attention due to its energy saving, lifetime, compactness and efficiency [2, 3]. Because of these advantages, we are experiencing a major paradigm shift where SSL has gained both commercial and scientific interest [4]. As a result, light emitting diodes (LEDs) have started to find wide-spread use for lighting applications in cars, homes, offices, streets and displays (see Figure 1). Due to the increasing efficiency and quality, LEDs have potential to replace with traditional lighting technologies and they are expected to be the dominant light source in the future. For example, the company of Forest Lighting owing 2.4% of LED market share, produces 20 billion units per month in 2014; moreover, its growth rate is increasing 1 billion units per month [5]. Therefore, it is evident that the total global production and consumption of LEDs will significantly increase in the near future by orders orders of magnitudes.

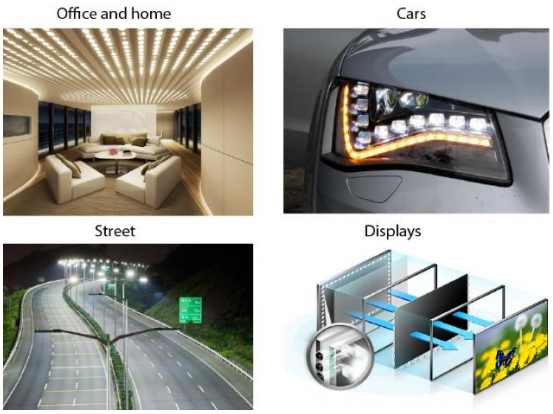

Figure 1. LED applications [6]

Today the enormous demand for electronics leads to massive amount of waste and decrease of scarce natural elements. For example, in 2011 approximately 3 million tons of e-waste was generated and only 24.9% of e-waste was recycled and the remaining amount of e-waste was trashed [7]. This remaining waste generate significant hazard to the environment (e.g., great pacific garbage patch (see Figure 2) [8]. Therefore, the integration of 'green' materials in electronics is important for environmental protection and sustainability.

Figure 2 Pacific garbage patch

Materials that are produced by nature or produced in the laboratory utilizing polymers, ceramics, metallic components and composite materials, which is suitable with biological systems are called biomaterials. These materials offer an extensive and sophisticated library, which are generated and optimized in a multi-million year process [9]. This library provides a wide range of ceramic, metal and polymer biomaterials that can be directly adapted to various technological applications. For example, ceramic biomaterials such as hydroxyapatite are used for orthopedic implants and dental applications; biopolymers such as polyhydroxyalkanoates (PHAs) are used in biomedical implants.

Recently, the utilization of biomaterials for electronics were started to reduce the e-waste. For example, fully degradable transient electronics is demonstrated by Rogers et al.[10] (see Figure 3a). Transient electronics device used biocompatible materials such as, silk, Mg, MgO and Si, where silk is used as a substrate, Mg as an electrode, MgO as a dielectric and Si as diode. Another example is fully degradable non-toxic battery is produced using biodegradable materials [11] (see Fig. 3b), in future these batteries have potential to be exchanged with current batteries. Moreover, flexible electronics on biodegradable nanofibril paper is also demonstrated [12] (see Fig. 3c). Research and development on biomaterials integrated devices is developing quickly, because of people's awareness to greenhouse effects and e-waste. Due to this, developments on biomaterials integrated devices has great impact on Earth and ourselves. These green electronic devices have the potential to decrease the use of conventional devices for e-waste problem and to provide unconventional demonstrations for photonic and electronic applications [13-16]. Therefore, there is an increasing interest in the utilization of biomaterials for photonic and electronic devices [12, 17-24].

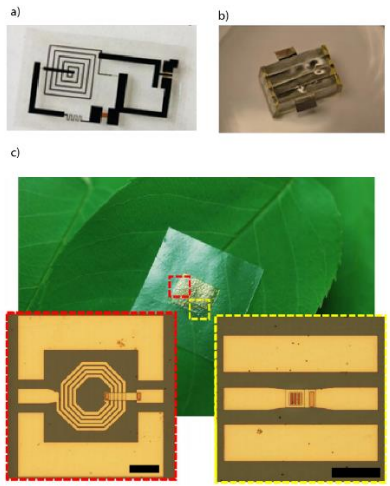

Figure 3 Examples of Transient electronics (a)Transient electronics using silk, Mg, MgO and Si[10] (b)Biodegradable battery[11] (c) Flexible electronics on nanofibril paper [12]

The transition of electronics from conventional materials to biomaterials is expected be analogous of the transition for plastic bags, which is already achieved. For example, 30

years ago polypropylene and polyethylene bags were used at a high amount, which was not eco-friendly and not biodegradable, and today the materials are replaced with polylactic acid, corn starch, jute and woven synthetic fibers, which are eco-friendly and fully biodegradable. Similar to this transition, we aim to transform the electronics from using conventional glasses, metals and plastics to biocompatible and biodegradable materials called “transient electronics” that will be absorbed by nature after their use.

In this thesis, proteins are explored for solid state lighting applications, such as color conversion layer and lenses. Two types of proteins are integrated on LEDs. Firstly, fluorescent proteins (FP) are used to make green, red and white LEDs. Their application to displays and daylight illumination is analyzed. Secondly, silk hydrogel was used as a lens for LEDs and its transmittance, radiation pattern and light extraction efficiencies are investigated.

In Chapter 2, general concepts about light sources is given attention to. Radiometric and photometric units are explained. CCT and CRI calculation methods are explained. Next, PN junction operation is stated. Finally, types of WLEDs are mentioned and specifically color conversion method is explained.

In Chapter 3, theoretical simulation in MATLAB on color mixing is analyzed. Single, double and triple FP mixing on blue pump LED is analyzed.

In Chapter 4, Color conversion is studied. From blue pump, green LED and from green pump, red LED is obtained. Combining white LED is obtained and its FRET is analyzed. Their application to displays and general lighting is analyzed.

In chapter 5, silk hydrogels are used to make lenses for light emitting diodes. Their transmittance, radiation pattern and light extraction efficiency are analyzed.

In chapter 6, thesis is summarized with conclusion.

Chapter 2 Background

2.1 General concepts about light sources

2.1.1 Technical concepts

In this sub-chapter the definition of technical concepts are explained.

Radiometric units: It is a physical property of electromagnetic radiation, which characterizes distribution of radiation power in space. The properties in radiometric units are defined in terms of photon energy (eV), number of photon and optical power (Watt).

Photometric units: Light and color perception of human eye is characterized by photometric units. For human eye each wavelength is weighted accordingly and the eye sensitivity function is used to transform the radiometric units to photometric units.

Eye sensitivity function: It converts radiometric units to photometric units. CIE 1931 (see Fig. 4) eye sensitivity function is V(λ) (e.g., V(λ=555nm) = 1). Eye sensitivity function reaches maximum at green and decreasing at blue and red regions of the visible spectra; hence, our eyes have low for red and blue colors. Sensitivity of human eye shift to blue spectrum due to adjustments of the cones and rods inside human eye

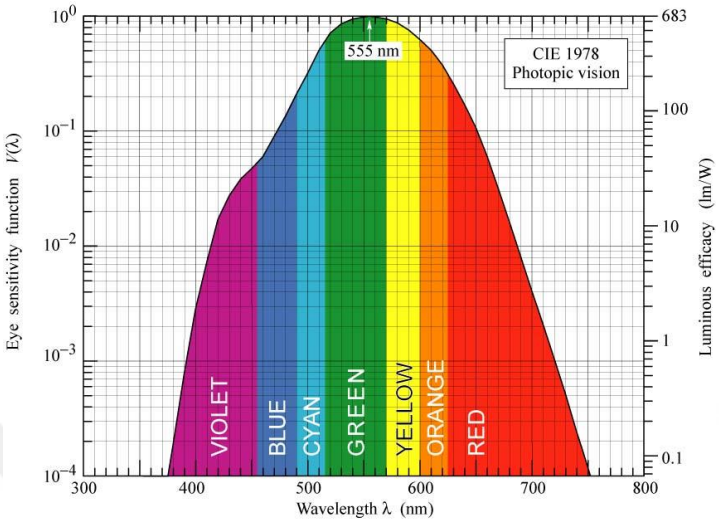

Figure 4. CIE1978 modified eye sensitivity function [25]

Luminous flux: It is a photometric quantity which is perceived light power by human eye. Its unit is lumen (lm). With power spectral density $P(\lambda)$. Luminous flux is:

$$\Phi_{lum} = 683\,{}^{lm}/_{W} \int V(\lambda)P(\lambda)d\lambda \qquad (1)$$

Illuminance: It is luminous flux per unit area. Its unit is lux (lm/m^2). Illuminance of full moon is taken to be 1 lux. Illuminance of direct sunlight is 5 order of magnitudes higher than that of moon.

Luminous efficacy of optical radiation: Optical power to luminous flux conversion efficiency is luminous efficacy. Its unit is $lm/W_{opt.}$ Luminous efficacy of optical radiation for different light sources are listed in Table 1.

Table 1. Luminous efficacy of optical radiation of light sources

Name	Luminous efficacy of optical radiation(lm/W)
candle	0.3
100–200 W tungsten incandescent (230 V)	13.8-15.2
Photographic and projection lamps	35
White LED	4.5-150
Light bulb	8-10
Fluorescent lamp	45-104
Metal halide lamp	64-115
Green light at 555nm (unity)	683

$$Luminous\ efficacy = {\Phi_{lum}}/{P} = \left[683\ {lm}/{W} \int V(\lambda)P(\lambda)d\lambda\right] / \int P(\lambda)d\lambda \quad (2)$$

Luminous efficiency: Electrical power to luminous flux conversion efficiency is luminous efficacy. Its unit is lm/$W_{elec.}$ In table ## Luminous efficiency for different light sources are listed in table 2.

Table 2 Luminous efficiency of light sources

Name	Luminous efficieny(lm/W)
Tungsten filament light bulb	15-20
Quart Halogen light bulb	20-25
Fluorescent light tubes	50-80
Mercury vapor light bulbs	50-60

Metal halide light bulbs	80-125
High-pressure sodium light bulbs	100-140

$$Luminous\ efficiency = {}^{\Phi_{lum}}/_{P} = \left[683\ {}^{lm}/_{W} \int V(\lambda)P(\lambda)d\lambda\right]/\text{IV} \quad (3)$$

2.1.2 Color matching function and chromaticity diagram

Human eye has red, blue and green cones to receive light, these cones are excited uniquely. Individuals can sense color and luminous flux slightly differently. Because of that, the International Commission for Illumination (CIE) came up with color matching functions (see Fig. 5) and the chromaticity diagram (CIE, 1931). $x(\lambda), y(\lambda)\ and\ z(\lambda)$ (see Fig. 5) are CIE 1931 color matching functions. Eye sensitivity function is same as green color matching function.

$$y(\lambda) = V(\lambda) \quad (4)$$

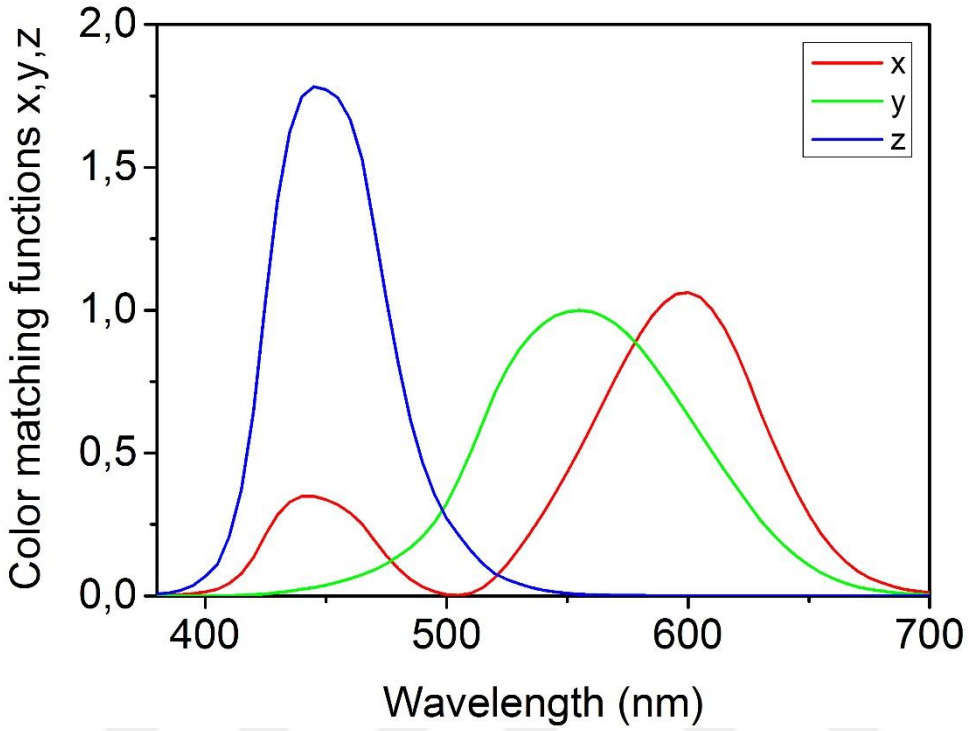

Figure 5 *Eye sensitivity functions x,y,z (CIE, 1931)*

For power spectral density $P(\lambda)$, X, Y and Z tristimulus values can be calculated in this order:

$$X = \int x(\lambda)P(\lambda)d\lambda \quad (5)$$

$$Y = \int y(\lambda)P(\lambda)d\lambda \quad (6)$$

$$Z = \int z(\lambda)P(\lambda)d\lambda \quad (7)$$

X, Y and Z are unitless. Using tristimulus coordinates, chromaticity coordinates can be calculated as follows:

$$x = X/(X + Y + Z) \quad (8)$$

$$y = Y/(X + Y + Z) \quad (9)$$

$$z = \frac{Z}{X+Y+Z} = 1 - x - y \quad (10)$$

In Fig. 6 chromaticity (x,y) can be seen.

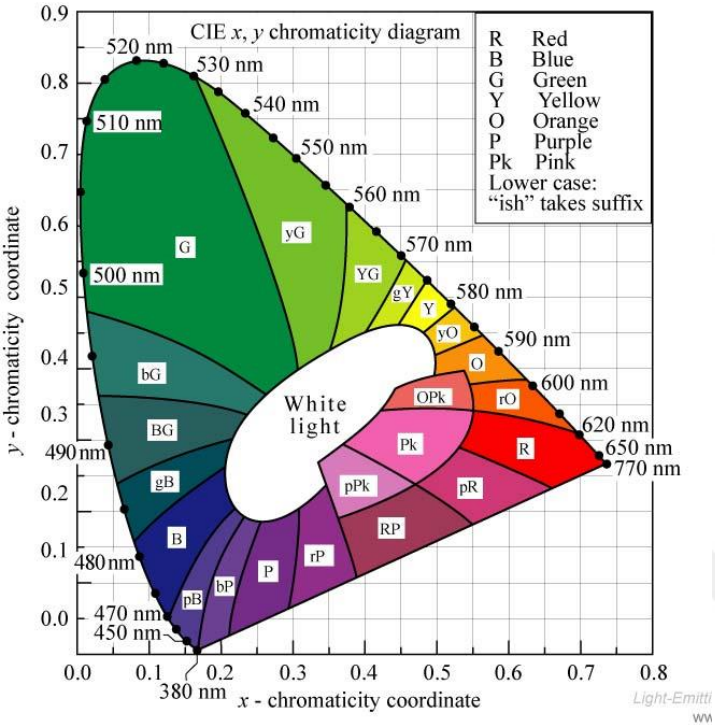

Figure 6. CIE 1931 chromaticity diagram with colors mapped. [25]

(x,y,z) = (1/3, 1/3, 1/3) is called equal point energy where optical spectrum has constant spectral distribution.

In CIE 1931 color space color difference is not proportional to geometric difference, hence, CIE 1960 (u,v) uniform chromaticity coordinates were introduced.

$$u = 4X/(X + 15Y + 3Z) \quad (11)$$

$$v = 6Y/(X + 15Y + 3Z) \quad (12)$$

CIE 1976 (u',v') uniform chromaticity coordinates are

$$u' = 4X/(X + 15Y + 3Z) \quad (13)$$

$$v' = 9Y/(X + 15Y + 3Z) \quad (14)$$

Conversion between (x,y) to (u,v) is as follows:

$$u = 4x/(-2x + 12y + 3) \quad (15)$$

$$v = 6y/(-2x + 12y + 3) \quad (16)$$

2.1.3 Color Temperature

The blackbody radiators are standard light sources to determine the color temperatures. This standard spectrum is defined by Planckian black-body radiation as follows:

$$I(\lambda) = \frac{2hc^2}{\lambda^5[\exp\left(\frac{hc}{\lambda kT}\right)-1]} \quad (17)$$

Black body radiation which is called planckian locus is located in the Fig. 7. Standard illuminants are A, B, C, D_{65} and E located on planckian locus in Fig. 7 and their color temperature are summarized in Table 3.

Table 3 Standard illuminants

Name	x – chromaticity coordinate	y– chromaticity coordinate	CCT(K)
A	0.44	0.40	2856
B	0.35	0.35	4874

C	0.31	0.32	6774
D_{65}	0.31	0.33	6504
E	0.33	0.33	5454

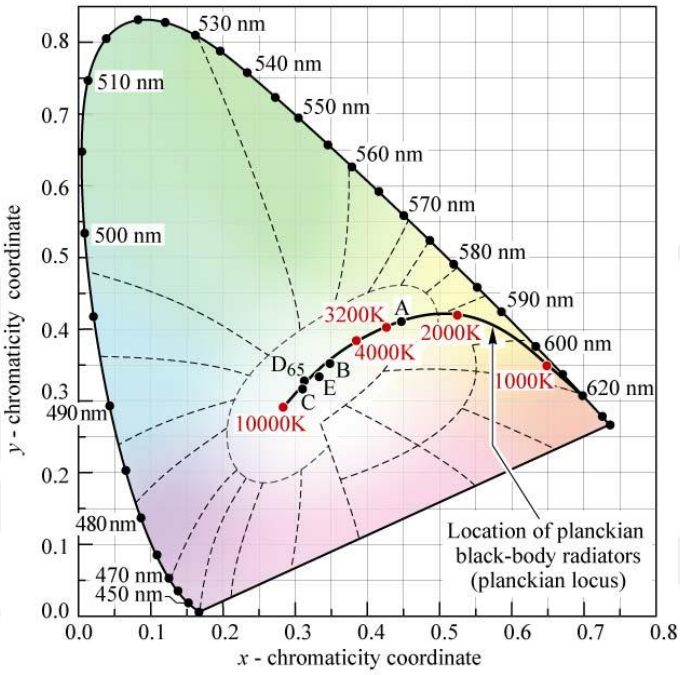

Figure 7. Chromaticity diagram showing planckian locus [25]

For light sources, which doesn't fall on planckian locus color temperature is defined with correlated color temperature (CCT). CCT is the nearest distant planckian locus to a white light source on (u',v') chromaticity diagram.

2.1.4 Color mixing

Additive mixing of more light sources is important to understand the resulting color combined by different sources. For example, two or more light sources mixed can result

in white light for LEDs. To obtain white LEDs commonly blue, green and red colors are mixed. Let's consider that there are three light sources emissions $P_1(\lambda)$, $P_2(\lambda)$ and $P_3(\lambda)$, their chromaticity coordinates are (x_1, y_1), (x_2, y_2) and (x_3, y_3). When three light sources are mixed, their tristimulus coordinates can be calculated as follows:

$$X = \int x(\lambda)P_1(\lambda)d\lambda + \int x(\lambda)P_2(\lambda)d\lambda + \int x(\lambda)P_3(\lambda)d\lambda = x(\lambda_1)P_1 + x(\lambda_2)P_2 + x(\lambda_3)P_3 \quad (18)$$

$$Y = \int y(\lambda)P_1(\lambda)d\lambda + \int y(\lambda)P_2(\lambda)d\lambda + \int y(\lambda)P_3(\lambda)d\lambda = y(\lambda_1)P_1 + y(\lambda_2)P_2 + y(\lambda_3)P_3 \quad (19)$$

$$Z = \int z(\lambda)P_1(\lambda)d\lambda + \int z(\lambda)P_2(\lambda)d\lambda + \int z(\lambda)P_3(\lambda)d\lambda = z(\lambda_1)P_1 + z(\lambda_2)P_2 + z(\lambda_3)P_3 \quad (20)$$

Chromaticity coordinates are as follows:

$$x = \frac{x_1L_1+x_2L_2+x_3L_3}{L_1+L_2+L_3} \quad (24)$$

$$y = \frac{y_1L_1+y_2L_2+y_3L_3}{L_1+L_2+L_3} \quad (25)$$

where

$$L_1 = x(\lambda_1)P_1 + y(\lambda_1)P_1 + z(\lambda_1)P_1 \quad (21)$$

$$L_2 = x(\lambda_2)P_2 + y(\lambda_2)P_2 + z(\lambda_2)P_2 \quad (22)$$

$$L_3 = x(\lambda_3)P_3 + y(\lambda_3)P_3 + z(\lambda_3)P_3 \quad (23)$$

When two colors are mixed, chromaticity coordinate will be located between source 1 and source 2 with straight line (see Fig. 8). Using 2 sources any color can be generated. When 3 colors are mixed, mixed color will be located in the triangle corners points being source chromaticity coordinates. The triangle obtained will be color gamut.

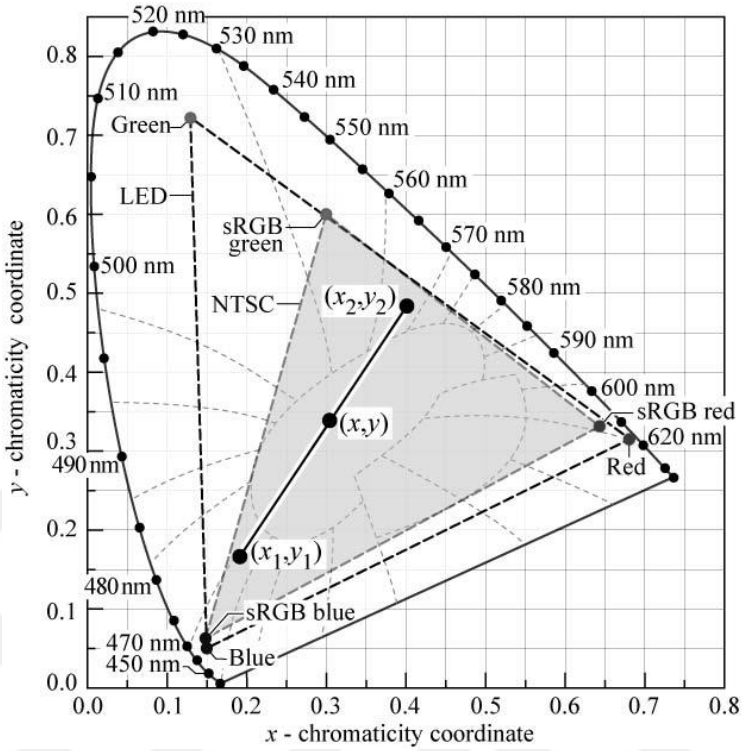

Figure 8. Color mixing and color gamut.[25]

2.1.5 Color rendering index

Color rendering index (CRI) measures the ability of a light source showing true color of a physical object. High color rendering index white light sources displays objects as more vivid and richer. Low CRI sources are used in streets, but high CRI sources in offices, museums and etc. Color-rendering ability is measure of how test light source has same color rendering ability with reference light source. CRI of planckian black-body radiator by convention is taken to be 100, which is the reference light source and has the highest value. CRI of other sources is less than 100, because it compares to planckian black-body radiator. In principle, the minimum achievable CRI is -100.

In this thesis below mentioned formulas are coded and CRI is calculated utilizing high speed computer using MATLAB.

To be able to calculate CRI, first of all reference source is chosen

1. If chromaticity coordinates of test source is on planckian locus, reference source is planckian black body radiator.
2. If chromaticity coordinates of test source is off planckian locus, reference source is planckian black body radiator with the same correlated color temperature as the test source.

There are 14 standardized test-color samples (see fig. 9). CRI is calculated as follows:

$$CRI_{general} = \frac{1}{8}\sum_{i=1}^{8} CRI_i \quad (26)$$

Where

$$CRI_i = 100 - 4.6\Delta E_i^* \quad (27)$$

Eight standard test-color samples are given in see fig. 9.

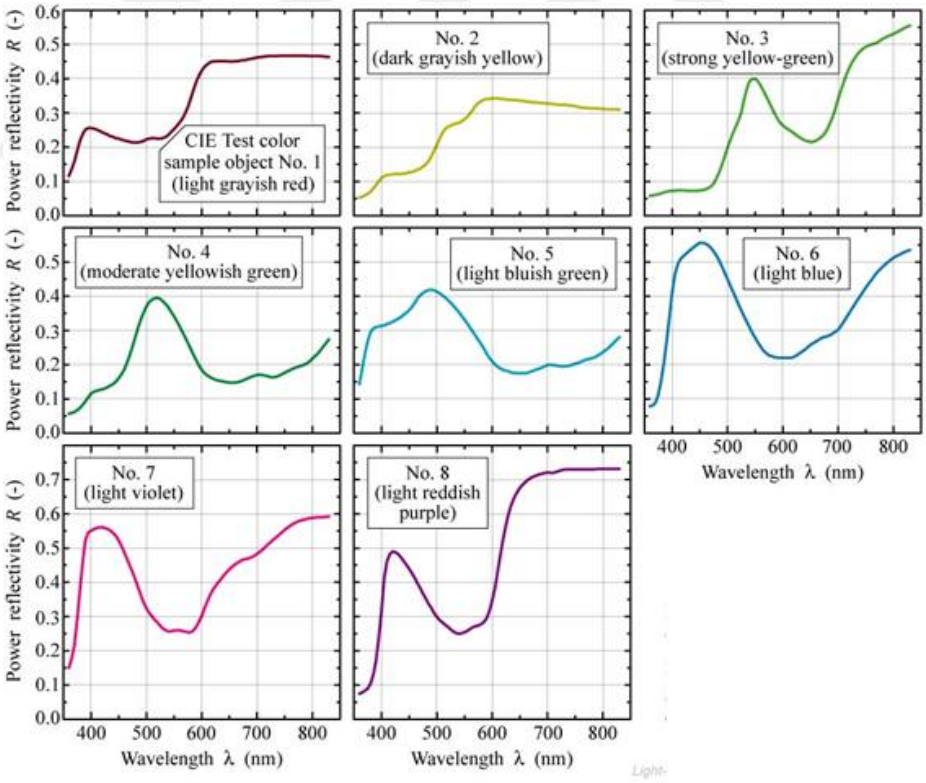

Figure 9. 8 standart sources.

Generally samples are off planckian locus. ΔE_i^* are calculated as follows. (c,d) coordinates are introduced.

$$c = (4 - u - 10v)/v \text{ (28)}$$

$$d = (1.708v + 0.404 - 1.481u)/v \text{ (29)}$$

There are 2 variables with 3 sources corresponding to 6 equations: (u_{ref},v_{ref}), (u_{test},v_{test}), ($u_{test,i}$,$v_{test,i}$), (c_{ref},d_{ref}), (c_{test},d_{test}) and ($c_{test,i}$,$d_{test,i}$). Adaptive-color-shifted coordinates of test-color samples are calculated as follows:

$$u_{test,i}^{**} = \frac{10.872 + 0.404\frac{c_{ref}}{c_{test}}c_{test,i} - 4\frac{d_{ref}}{d_{test}}d_{test,i}}{16.518 + 1.481\frac{c_{ref}}{c_{test}}c_{test,i} - \frac{d_{ref}}{d_{test}}d_{test,i}} \text{ (30)}$$

$$v_{test,i}^{**} = \frac{5.520}{16.518 + 1.481\frac{c_{ref}}{c_{test}}c_{test,i} - \frac{d_{ref}}{d_{test}}d_{test,i}} \text{ (31)}$$

Adaptive-color-shifted coordinates of test source are calculated as follows:

$$u_{test}^{**} = \frac{10.872 + 0.404c_{ref} - 4d_{ref}}{16.518 + 1.481c_{ref} - d_{ref}} = u_{ref} \text{ (32)}$$

$$v_{test}^{**} = \frac{5.520}{16.518 + 1.481c_{ref} - d_{ref}} = v_{ref} \text{ (33)}$$

At last color difference is calculated from uniform color space coordinates.

$$\Delta E_i^* = \sqrt{(\Delta L^{**})^2 + (\Delta u^{**})^2 + (\Delta v^{**})^2} \text{ (34)}$$

Where

$$\Delta L^{**} = L_{ref,i}^{**} - L_{test,i}^{**} = \left[25{Y_{ref,i}}^{\frac{1}{3}} - 17\right] - \left[25{Y_{test,i}}^{\frac{1}{3}} - 17\right] \text{ (35)}$$

$$\Delta u^{**} = u_{ref,i}^{***} - u_{test,i}^{***} = 13L_{ref,i}^{**}\left(u_{ref,i} - u_{ref}\right) - 13L_{test,i}^{**}\left(u_{test,i}^{**} - u_{test}^{**}\right) \text{ (36)}$$

$$\Delta v^{**} = v_{ref,i}^{***} - v_{test,i}^{***} = 13L_{ref,i}^{**}\left(v_{ref,i} - v_{ref}\right) - 13L_{test,i}^{**}\left(v_{test,i}^{**} - v_{test}^{**}\right) \text{ (37)}$$

2.2 FRET

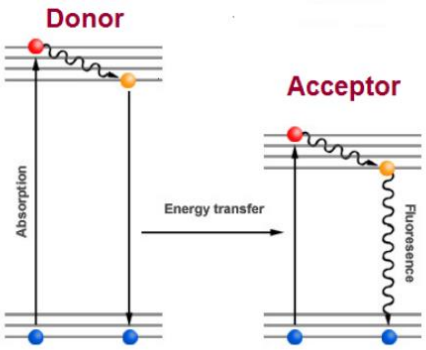

Figure 10 Jablonski diagram [26]

Energy transfer between two chromophores is called fluorescence resonance energy transfer (FRET) mechanism (see figure 10). In Fig. 11 emission of 2 fluorophores are given. Fluorophore 1 is donor and fluorophore 2 is acceptor. If the distance between two fluorophores is small (see figure 1 B1) FRET mechanism is not observed, however when these fluorophores are near each other FRET mechanism is observed (see figure 1 B1), where emission of fluorophore 1 is decreased and emission of fluorophore 2 increases (see figure 1 B1), due to the transfer of holes and electrons to the higher and lowers bands. For example, CFP/YFP is the common conjoint FRET pairs for biological applications. It is used as protease cleavage assay, where before protease cleavage due to FRET UV excited FPs emit yellow. However due to protease cleavage YFP is removed and under UV excitation cyan is emitted.

FRET efficiency E is:

$$E = \frac{k_{ET}}{k_f + k_{ET} + \sum k_i} \quad (38)$$

Where k_{ET} is rate energy transfer, k_f is radiative decay rate and k_i is the rate constant of de-excitation pathways. E depends on distance between donor and acceptor in a r^{-6} due to dipole-dipole coupling. In this thesis study FRET efficiency is calculated by lifetime measurements.

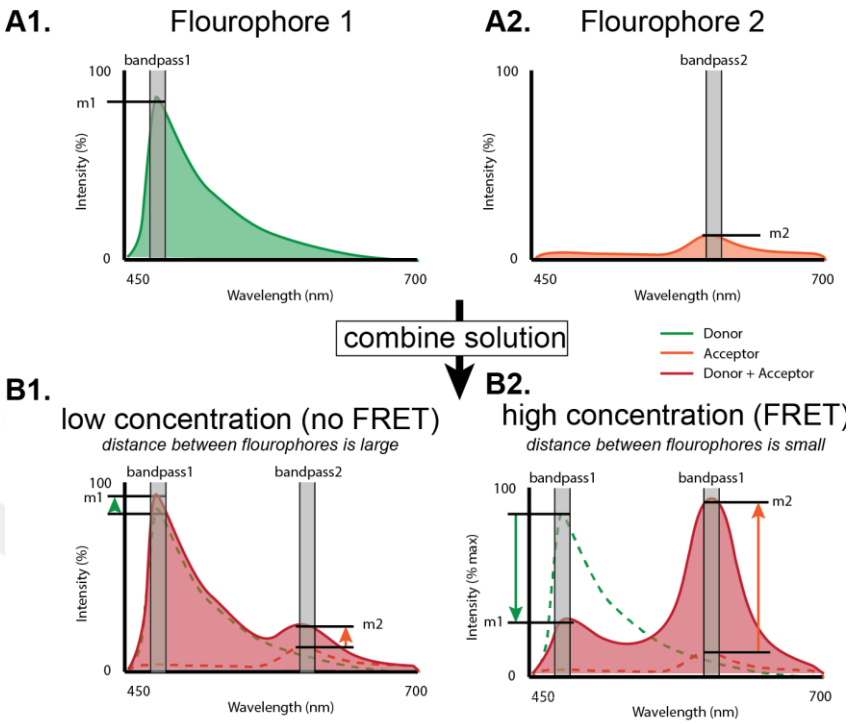

Figure 11. FRET mechanism

2.3 Semiconductor fundamentals of LEDs

Doping impurities in a pure semiconductor crystal, results concentration of electron or hole carriers, which is called extrinsic semiconductors. Doping pentavalent impurities in silicon crystal, which has four valence electrons, such as phosphorous and arsenic, yields n-type semiconductor, where electrons are majority carriers. When dopants generate electrons and results n-type semiconductors it's called donors. Whereas, doping trivalent impurities in silicon crystal, such as boron, yields p-type semiconductor, where holes are majority carriers. When dopants generate holes and result p-type semiconductors it's called acceptors. In Fig. 12 we can see crystal structure of silicon and doped arsenic atoms

have one electron not attached to atom and in Fig 12 b bandgap of silicon crystal and arsenic atom donating electrons to conduction band. Similarly, in Fig 13 a boron doped silicon crystal bonds accepts electron, hence hole is created. In Fig 13 b, boron is accepting electron from valence band, thus creating holes in valence band.

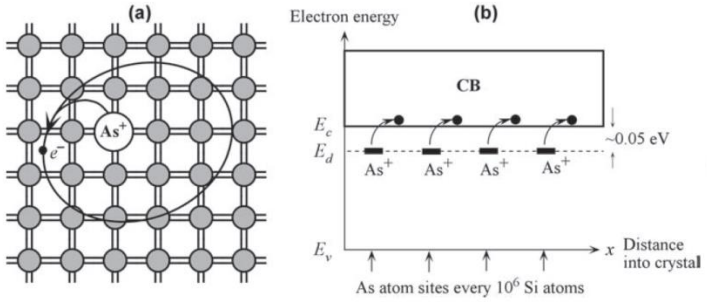

Figure 12. a) Arsenic in silicon crystal structure giving one electron. b) Bandgap of silicon where arsenic donates electron. [27]

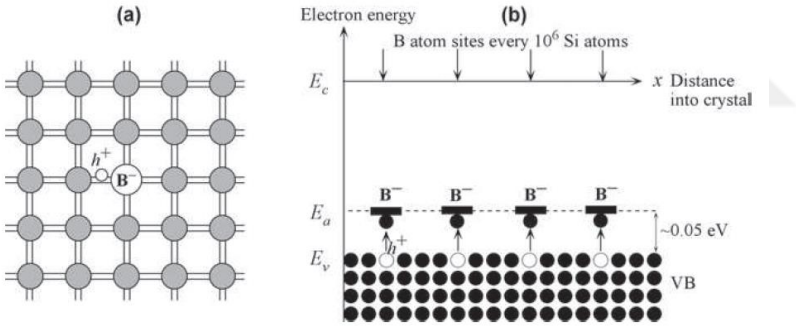

Figure 13 a) Boron in silicon crystal structure. b) Bandgap of silicon where boron donates holes [28]

When silicon crystal structure is doped, its Fermi level is changed according to type of the dopant. When a crystal structure is not doped Fermi level is approximately between valance and conduction energy levels (see Fig. 14a). Whereas, when semiconductor is doped with donors its Fermi level is near conduction band (see Fig. 14b). Acceptor doped silicon crystals Fermi level is near valence band.

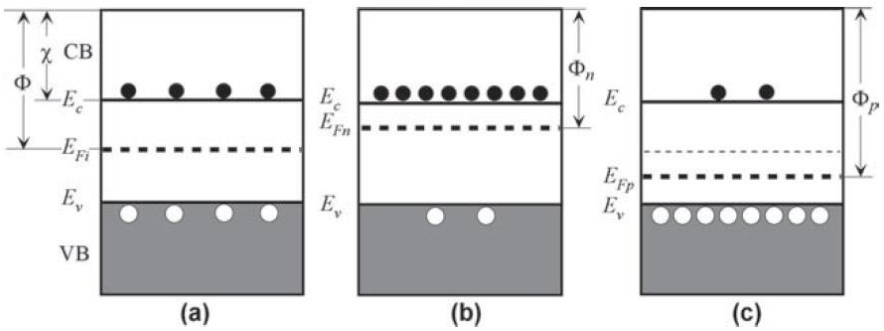

Figure 14 Energy band diagram. a) Intrinsic semiconductor b) n-type semiconductor c) p-type semiconductor. [28]

When p-type and n-type semiconductors are contacted, where pn connection is called metallurgical junction, in p-side ionized acceptor atoms and holes and in n-side ionized donor atoms and electrons exists. After contacting at metallurgical junction electrons and holes recombine, resulting acceptor ions in p-side and donor cations in n-side, thus creating space charge layer (SCL). It is also known as depletion region. This ions and cations creates internal electric field. Thus creating energy difference in energy band diagram. Under zero bias due the internal electric field energy band diagram can be seen in Fig. 15 a. When forward bias is applied total electric field is decreased. Thus, it is easier for electrons and holes to recombine due to diffusion of majority carriers. By this method LEDs are operated and light emitting is called electroluminescence.

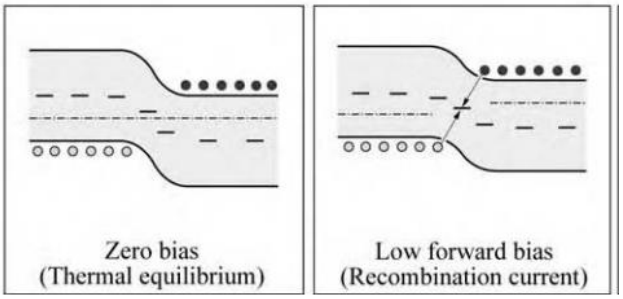

Figure 15 Energy band diagram of pn junction. a) Zero bias b) Forward bias c) Reverse bias [28]

To increase efficiency of light generation for forward biased pn junction, heterojunctions are used. The aim of heterojunction structures is to confine electrons and holes, such that probability of them recombining is increased. Another method to increase the efficiency

is using quantum wells sandwiched between two higher energy band diagram crystals. This way electrons and holes are recombined. In figure 16, Single quantum well is sandwiched between semiconductor crystals and its energy band is shown. Moreover to increase light output power multi quantum well structures are used. MQWs are commonly used for blue LEDs

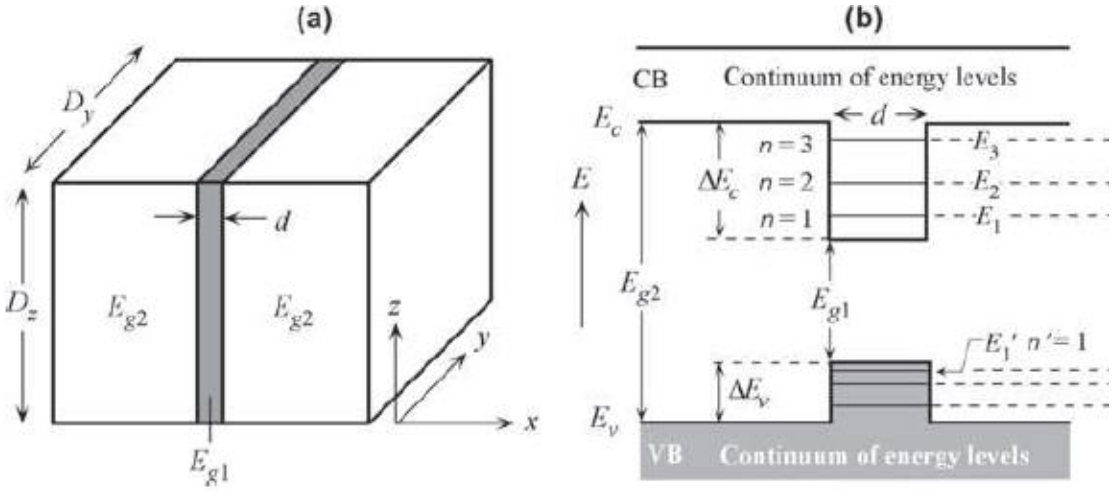

Figure 16 a) Single quantum well sandwiched between two higher energy band diagram semiconductor crystals. b) Energy band diagram and energy levels in single quantum well [28]

In this thesis, LEDs are operated in forward biased mode and their electroluminescence is used to pump the fluorescent proteins.

2.4 WLEDs

High efficiency, high power capability, good color rendering capability, high reliability and low-cost manufacturability are main properties of white LEDs (WLEDs) [25]. To date there are three main approaches to produce WLEDs, which are multichip WLEDs, monolithic WLEDs and color conversion WLEDs.

2.4.1 Multichip WLEDs

Multichip WLEDs is mounted in one package with many multiple emitters. Blue, green and red LEDs are used as emitters on a single package. Blue and green LEDs use InGaN emitters and red LEDs use AlGaInP emitters [29]. In figure 17 we can see PCB mounted multichip WLED. It has red, green and blue LEDs, combining intensity from each LEDs will result in white light from multichip WLED. Disadvantages of WLEDs are many LEDs put nearby heat the device, thus making it inefficient.

Figure 17 Multichip WLED RGB chips

2.4.2 Monolithic WLEDs

In monolithic WLEDs, multicolor emitting multiple-quantum wells (MQW) are used as active layers (see Fig. 18 a). InGaN as MQW is popular for covering visible region, hence they are used extensively. For example, in figure 18, blue and yellow stacked GaInN/GaN MWQ is used in monolithic device, which has peaks at 440 nm and 540 nm, thus combination of these two spectra results white light. The strong drawback of monolithic devices are with injected current, quality of the white light changes, thus these devices should be operated under constant and pre-defined current.

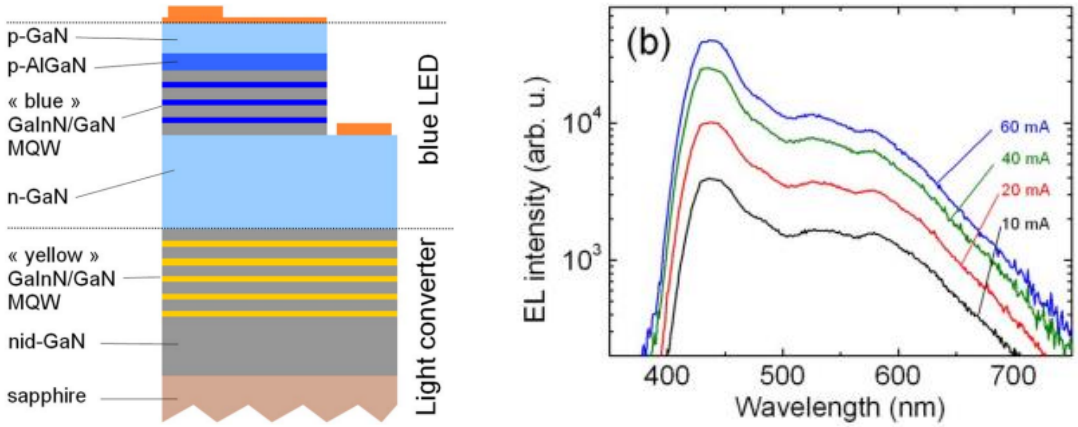

Figure 18 Monolithic WLEDs and its emission spectra for various currents [30]

2.4.3 Color conversion WLEDs

This Nobel Prize winning approach [31] is the most common among the three white light generation methods. In this method, materials such as dyes, polymers, phosphors and nanocrystals are used as wavelength converters. These materials are integrated on LEDs and use LED as a pump. Electrically driven LEDs emit light by electroluminescence and color converting materials are excited by photons and illuminate. Thus, electroluminescence of LED and photoluminescence of wavelength converting materials generate white light.

Color conversion WLEDs as well can be classified into four general groups according to materials they use for color conversion:

1. Dyes
2. Polymers
3. Phosphor
4. Nanocrystals

2.4.3.1 Dye based WLEDs

Dye based WLEDs use organic dyes as color conversion layer. For example, diphenylamine-substituted coumarin, (dicyanomethylene)-pyran, and benzophenoxazone are color converting dyes [32]. In these devices common cathode is used and blue emitter excites dyes and generally red and green emitting dye combined with blue emission results white light. Finite lifetime of these dyes are their main drawback, because they will bleach. When material becomes optically inactive they will become bleached. Generally lifetime of dyes are about 10^4-10^6 optical transitions.

2.4.3.2 Polymer based WLEDs

Conjugated polymers, such as (poly-paraphenylene) (m-LPPP) blue emitting and poly-perylene-co-diethynylbenzene) (PPDB) red emitting, are used for color conversion layer [33] for n-UV and blue pumps with high quantum efficiency on the order of 10^5 cm^{-1}. These polymers are coated with simple techniques such as spin and dip coating. The main drawback of these polymers are long-term stability problem.

2.4.3.1 Phosphor based WLEDs

Inorganically doped optical active elements are called phosphors. YAG phosphors have yttrium aluminum garnet (YAG) and they are mostly used to generate white LED. With optically active dopant they have broad emission from green to red spectra. Rare-earth elements, oxides and compounds are used as an optically active dopants.

Nakamura's invention of InGaN/GaN LED, which combined with phosphor color conversion revolutionized the SSL era. Blue luminescence of LED chip and phosphorescence of phosphor, generates white light (see Fig. 19). Blue LED driven white

light devices with yellow phosphor have high luminous efficacy, but it has low CRI. Whereas, UV driven white light devices with blue and yellow phosphors have high CRI; however, they have low efficiency. The disadvantages of phosphor based WLEDs are low color rendering index and they are not biocompatible and biodegradable.

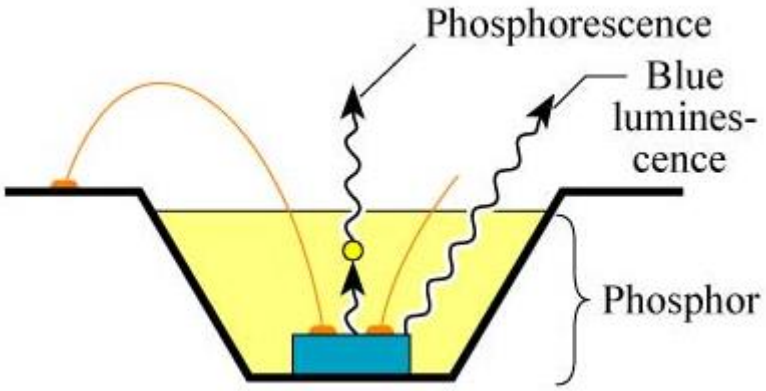

Figure 19 phosphor based WLEDs[25]

2.4.3.2 Nanocrystal based WLEDs

Quantum dots are nanosize crystals which convert light from lower wavelength to higher wavelength. The size ranges from 2-10 nm. With size quantum dots emits at different wavelengths. For example, CdSe/ZnS core-shell nanocrystal with 4 nm diameter emit at green.

Combination of different sizes nanocrystals on pump LED can generate WLED by photoluminescence of quantum dot nanocrystals. With size of nanocrystals white light parameters are finely adjusted. However, Cd based nanocrystals are toxic and compatibility of these nanocrystals with silicone matrix is a challenge.

2.5 Proteins

Proteins are building blocks of life, which are large macromolecules, consisting of long chains of amino acid residues. Sequence of amino acids make proteins distinguish from each other [34].

In this study green fluorescent protein (GFP) and red fluorescent protein (RFP) are used for color conversion and silk fibroin protein for making lenses for LEDs.

2.5.1 Fluorescent proteins

Green fluorescent proteins discovered in 1960 opened to new era with variety of applications , such as imaging of living cells and tissues[34, 35]. General weight of all fluorescent proteins (FPs) are 25 kD. The FP resembles cylindrical structure (see Fig. 20). In this thesis for simulation 12 FPs are used and for experimental 2 FPs used. Quantum efficiency are given in table 4.

Table 4. Quantum Yields of FPs

Name	Quantum efficiency
CFP	0.4
Citrine	0.76
dTomato	0.69
eGFP	0.6
mBanana	0.7
mCherry	0.22
mHoneydew	0.12

mOrange	0.69
mPlum	0.1
mStrawberry	0.29
mTangerine	0.3
Sapphire	0.64

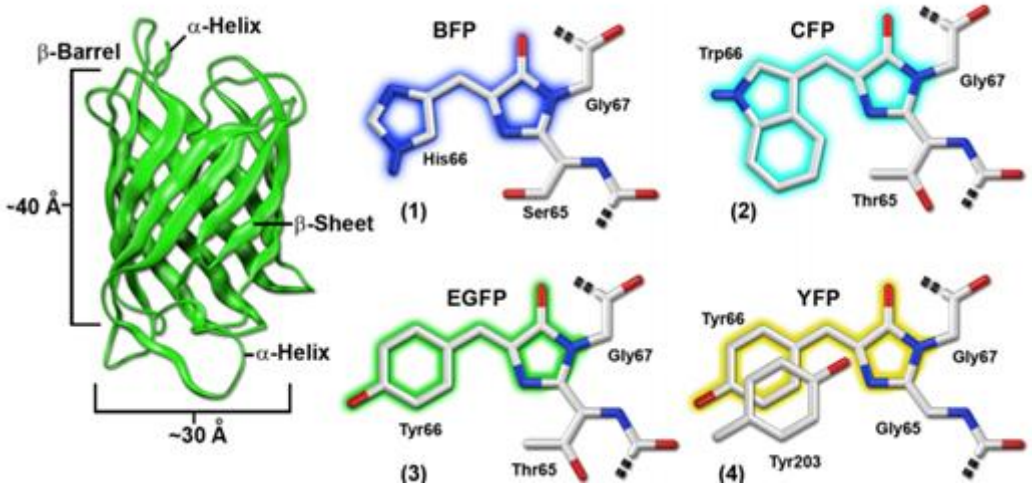

Figure 20. Structure of fluorescent protein. 1) BFP 2) CFP 3) EGFP 4) YFP [36]

Absorption and Emission of 12 FPs are given in Appendix 1.

Chapter 3 Color conversion using FPs

In this chapter we investigate theoretical simulation of FPs to understand attainable maximum CRI and its spectra. Single, double and triple FPs are used with blue pump LED. Afterwards vectors, expression and purification of fluorescent proteins and its spectroscopy is analyzed. Then, green, red and white LEDs are produced using eGFP, mCherry, blue and green LEDs. WLEDs FRET, application to displays and general lighting is analyzed.

3.1 Introduction

Lighting devices have been a major contributor to today's modern society that extend the daily activities throughout the timeframes and places without natural sunlight [37]. Solid-state lighting (SSL) has attracted a great deal of attention because of its important benefits including energy saving, safety, reliability and maintenance relative to other technologies (e.g., light bulbs, fluorescent lamps, etc.) [38, 39]. Today the dominant white LED technology is based on the color-conversion approach that uses the inorganic phosphor, Ce:YAG integrated over GaN blue LED chips [31]. However, the broad emission band of the phosphor limits the fine tuning of the white emission spectrum. Moreover, there are concerns over the global supply of the rare earth elements required to produce the Ce:YAG phosphors [40]. One possible way to overcome these limitations is to use

nanocrystal quantum dots (QDs) as an addition or replacement for the phosphor [41]. One of the most investigated QDs for color-conversion LEDs are CdSe/ZnS core/shell structures. However, their chemical synthesis in general require relatively high temperatures ranging from 100 to 300^{o}C and their toxic heavy metal content limits them for replacement [42-45]. Although relatively non-toxic nanocrystals such as InP/ZnS core/shell QDs [46] have been investigated, there are still concerns about the intrinsic toxicity of nanocrystals that may limit their applications [47].

Alternatively, we use fluorescent proteins as color-conversion materials for LED technology. Different from the previous study combining fluorescent proteins with synthetic rubbers [48], we made color-conversion layers solely from bio-derived proteins. In this study, we demonstrated white LEDs with color-rendering indices (CRI) above 80 for general lighting and their use in a 3.5" liquid-crystal display television (LCD TV). Furthermore, we control and tune the photometric properties via fluorescent protein density, and show warm, daylight and cool white LEDs. Fluorescent proteins offer advantageous properties for use in LEDs. In this study, we describe the synthesis and purification of enhanced GFP (eGFP) and monomeric Cherry (mCherry) proteins in *Escherichia coli*, and their integration onto LED chips. All the processes in the synthesis of these biomaterials, from bacterial expression to purification, take place at physiological temperatures. Moreover, the eleven-stranded barrel shape of these proteins, with the photoactive moiety at the center, suppress non-radiative energy transfer between

active centers, and this allows them to be used at high concentrations without significant degradation in their optical properties [49]. In addition, the ecological diversity and bio-engineering of fluorescent proteins also allows us to choose among a variety of phenotypes that span the entire visible spectrum ranging from blue to red [50, 51]. The combination of a large color palette with narrow emission bands allow for tunable white light generation. These favorable properties make fluorescent proteins promising wavelength-converters for LED applications.

3.2 Numerical Simulation of FPs

The initial attempts based on various color-converters are shown and experimentally the luminous efficacy of optical radiation can go upto 404 lm/W. Recently the theoretical limit of a ultra-efficient inorganic solid state lighting sources was investigated. According to that study, four components (RYGB) with 1nm linewidth is used. RYGB components had intensity at 614, 573, 530 and 463 nm. It is possible to obtain CRI of 90, CCT of 3000 K and LER of 408 lm/W [37]. Therefore, solid state lighting because of high optical parameters hold great promise.

As discussed in Chapter 1, fluorescent proteins hold great promise for future lighting applications because of their biocompatibility, and spectral tunability. Here, we investigate photometric study of superposition of 12 FPs emission spectra (Appendix 1) with pump blue LED with MATLAB. CCT, LER and CRI calculator was coded in MATLAB to understand the limits of fluorescent protein integrated white LED technology. Optical parameters including emission spectra of FPs, relative amplitude of each FP color component, their possible spectral peak and linewidth shift while integrating on LED chips and pump blue LED spectra are carefully designed to achieve highest-quality white light generation. Moreover, trade of photometric parameters using

up to 214375 samples are investigated. In the simulation we neglected the spectral change due to optical absorption and re-absorption processes. Emission of FP are uploaded in MATLAB and sampled to 5nm intervals. Then FP and blue is superposed, where their relative intensity and peak amplitude shift is taken, to obtain the white light. The spectral and the emission spectral shape of FPs doesn't changes, its peak is red shifted up to 30 nm.

CCT, LER and CRI are coded in MATLAB using formulations explained in Chapter 2. In this simulation, emission spectra of FPs (see appendix 1 for absorption and emission spectra) is numerically imported into MATLAB. We had 12 FP spectra where its peak ranged from cyan to red in visible spectrum. It was assumed that FWHM doesn't change due to reabsorption for simplicity and new computational code will be designed to encompass more optical phenomena such as reabsorption and FRET in future work. Amplitude of each spectra varied between 1 and up to 200. Superposing blue pump LED and one, two and three FP white light is generated and up to 214375 possible emission spectra were generated and investigated.

3.2.1 Single FP color conversion

To obtain white color, two-color mixing is used, which combines the electroluminescence of LED chip and photoluminescence of fluorescent proteins. Blue LED chip is the source, which has peak wavelength at 465 nm and full-width-half-maximum (FWHM) of 17 nm (see Fig. 21). Green fluorescent protein (eGFP), red fluorescent protein (mCherry) and mHoneydew FP (see Appendix 1 to see the spectrum of eGFP, mCherry and mHoneydew FPs) was utilized with blue LED chip.

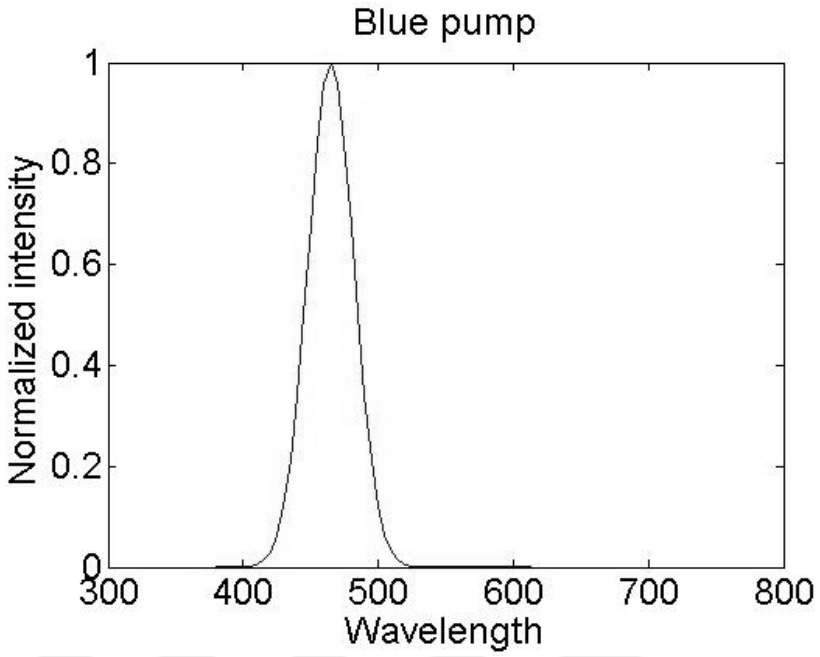

Figure 21. Blue pump

Table 5 Highest CRI obtained using MATLAB simulation for single FPs.

FP	Highest CRI
eGFP	50
mBanana	64
mCherry	60
mHoneydew	76

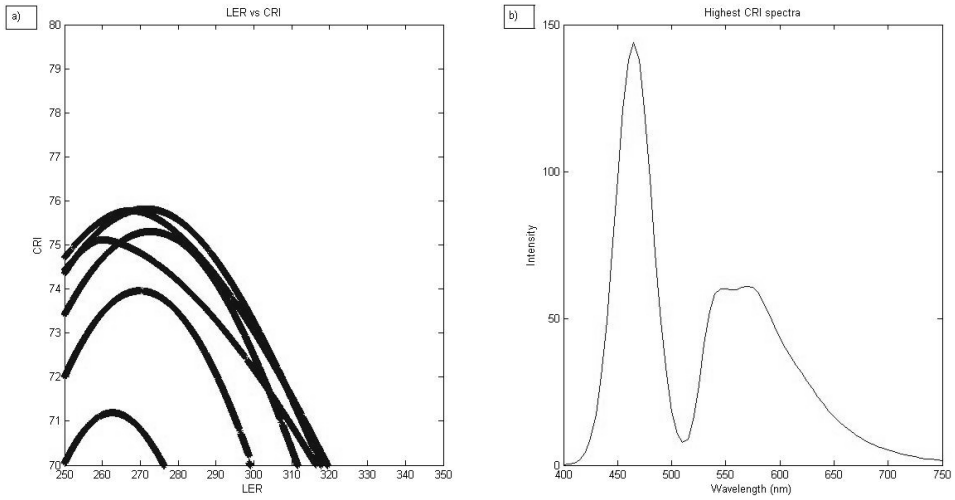

Figure 22. Single FP color conversion. a) LER vs CRI plot b) best CRI sample. Total number of simulated spectra is 100.000.

In table 5 the highest possible CRI with single color-converting FPs are shown. Among 4 exclusive FPs, mHoneydew had the highest FWHM and covers green and red spectrum. Hence, for single FP color conversion, mHoneydew is the best choice. Highest CRI with single FP was 76 with the chromaticity coordinate of (0.28, 0.27) and a CCT of 1042 K. It is observed that there is a trade of between CRI and LER. For two-color mixing white light generation for CRI>70, the maximum obtainable LER is 319 lm/W and the CRI vs LER and best CRI spectra is shown is fig. 22.

To summarize, with single FP color conversion high CRI was not obtained. Hence, double FP conversion is investigated for higher CRI.

3.2.2 Double FP color conversion

Since for two color mixing high CRI levels were not obtained, three color mixing is investigated. For this, the combinations of blue pump source, eGFP and mCherry are used

and above hundred thousand spectra are simulated. It is observed that there is a trade of between CRI and LER. For three color mixing while white light generation for CRI is higher than 70, maximum achievable LER is 400 lm/W (see Figure 23a). Highest CRI for double FP color conversion was 94 with (0.34, 0.35) chromaticity coordinates and 5040K CCT (see the spectrum in Figure 23b).

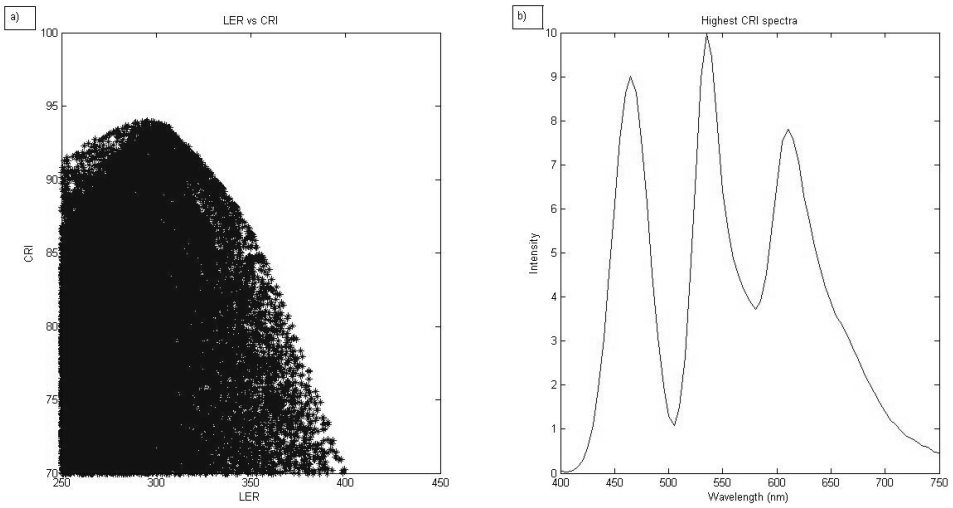

Figure 23. Double FP color conversion. a) LER vs CRI plot b) best CRI sample. Total number of simulated spectra is 214375.

To conclude, 94 is very high CRI; however, to obtain even higher quality white light third FP needs to be used so that CRI could reach even higher number.

3.2.3 Triple FP color conversion

Three color mixing resulted very high CRI, however to reach the limit, four color mixing is investigated using MATLAB. mBanana was used (see Appendix 1) with blue pump, eGFP and mCherry and above hundred thousand spectra are simulated. It is observed that there is a trade of between CRI and LER. For three color mixing while white light generation for CRI is higher than 70, maximum achievable LER is 404 lm/W (see Figure

24a). Highest CRI for triple FP color conversion was 98 with (0.45, 0.41) chromaticity coordinates and 2870K CCT, which is excellent (see the spectrum in Figure 23b).

.

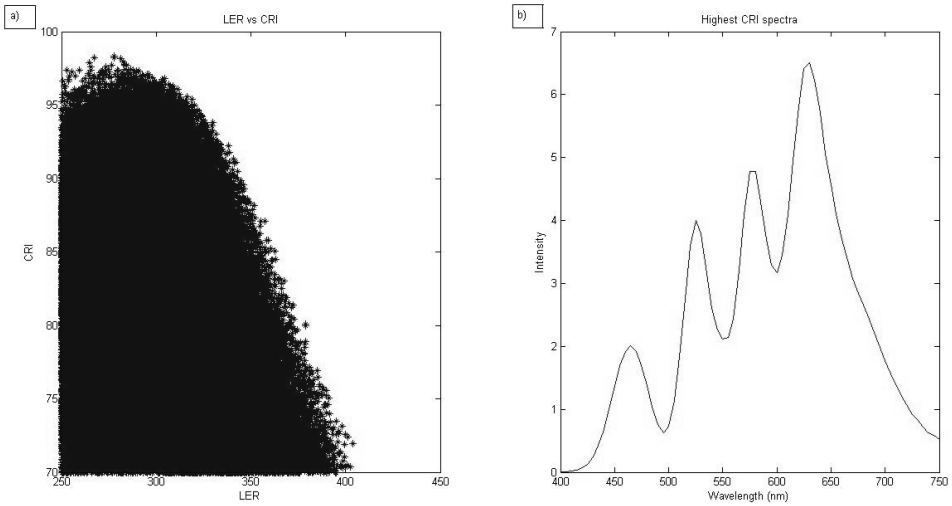

Figure 24. Triple FP color conversion. a) LER vs CRI plot b) best CRI sample. Total number of simulated spectra is 165375.

To conclude, 98 is excellent CRI. Best CRI spectra resembles the Planckian black-body radiation pattern.

3.3 Fluorescent protein preparation

3.3.1 Fluorescent protein vectors

The eGFP-GST fusion protein vector was present in a pGEX vector encoding for the 30 kDa eGFP N terminally linked to the 26 kDa GST; giving a 56 kDa molecular weight protein.

The mCherry-GST fusion protein vector was present in a pDEST vector encoding for the 26.7 kDa mCherry N terminally linked to the 26 kDA GST; giving a 52.7 kDa molecular weight protein.

3.3.2 Fluorescent proteins expression and purification:

eGFP and mCherry were expressed and purified using the *E. coli* expression system. Fluorescent proteins were expressed in *E. coli* BL21-Rosetta cells grown to OD600 = 0.6 and induced with 1 mM isopropyl β-d-1-thiogalactopyranoside for 2 days at 30°C. Following expression, bacteria were pelleted and lysed by freeze–thaw and sonication with 1 mg/ml lysozyme in glutathione *S*-transferase (GST)–binding lysis buffer (1× phosphate-buffered saline [PBS; 137 mM NaCl, 2.7 mM KCl, 8 mM Na2HPO4, 1.46 mM KH_2PO_4], pH 7.4, 250 mM KCl, and protease inhibitors 10 μg/ml each of aprotinin, leupeptin, pepstatin, and 1 mM phenylmethylsulfonyl fluoride]). The proteins were purified by affinity chromatography using glutathione–sepharose beads (Thermo Scientific). Recombinant proteins were eluted from the beads with elution buffer (50 mM Tris pH 8.0, 10 mM glutathione, 10 mM DTT supplemented with protease inhibitors) and the pooled eluates were run through the 10,000 NMWL centrifugal filters (Amicon® Ultra-4) for buffer exchange and concentration. The expression of recombinant proteins was confirmed by Coomassie Blue gel staining.

3.3.3 Spectroscopy of FP

Absorption and emission spectra were acquired with a Fluoromax 3 (HORIBA, Ltd; Kyoto, Japan) for solutions of eGFP and mCherry (see Figure 25d).

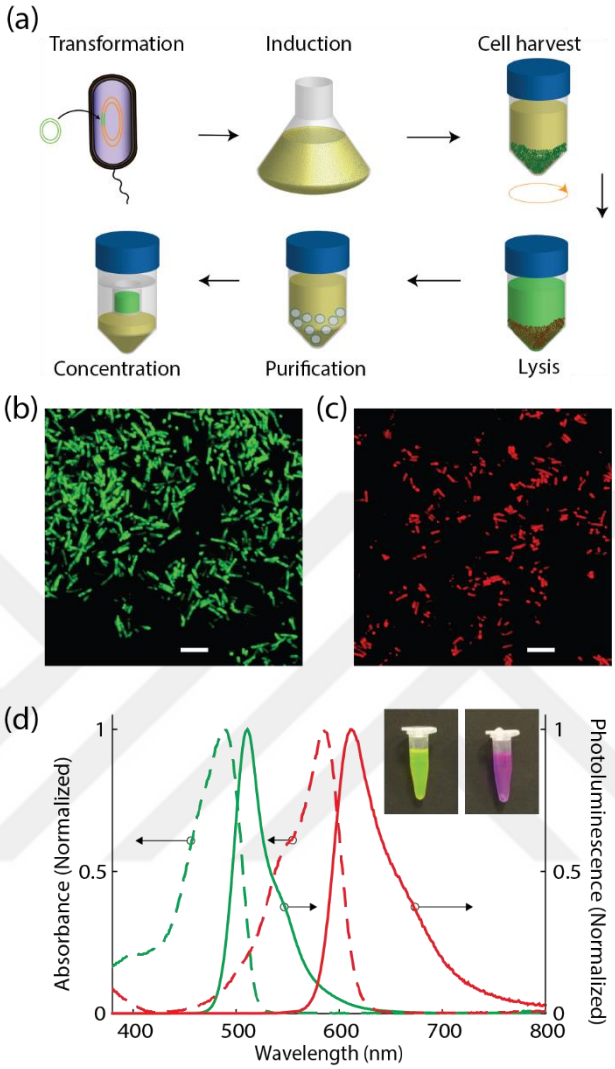

Figure 25*(a) Expression and purification of fluorescent proteins in* Escherichia coli (E.coli). *(b) Fluorescence image of an eGFP expressing* E.Coli *colony. (c) Fluorescence image of an mCherry expressing* E.Coli *colony. Scale bars (b) and (c) are 6 µm. (d) The absorption (dashed lines) and photoluminescence (solid lines) spectra of eGFP (green) and mCherry (red) solutions. The insets show eGFP (on the left) and mCherry (on the right) solutions under white light.*

The emission properties of the pump LEDs were determined with a fiber coupled CCS200 Compact Spectrometer (Thorlabs; NJ, USA). Blue pump LED has a peak wavelength of 465 nm and full-width-half-maximum (FWHM) of 17 nm, and green pump LED has a

peak wavelength of 535 nm and full-width-half-maximum (FWHM) of 22 nm at current injection levels of 10 mA (see Figure 26).

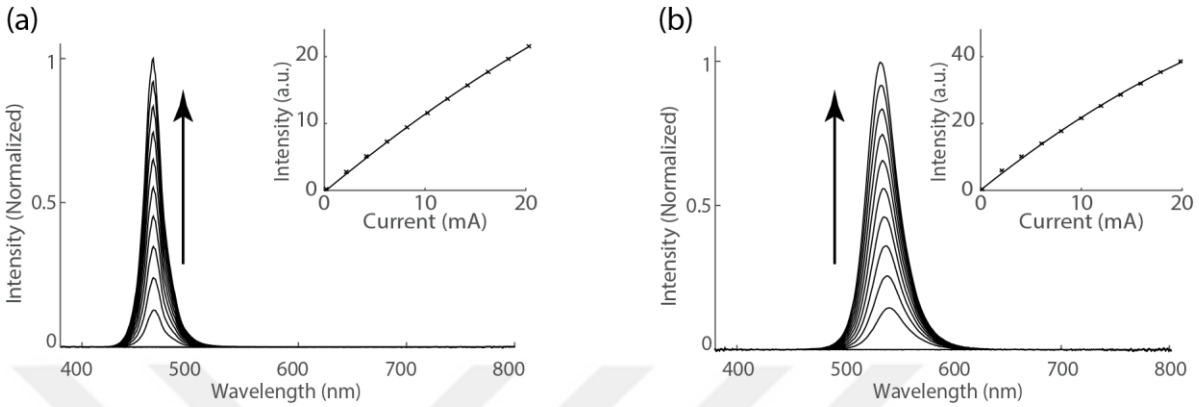

Figure 26. (a) The spectra of the blue pump LED with increasing current bias. The inset shows the total integrated intensity. (b) The spectra of the green pump LED with increasing current bias. The inset shows the total integrated intensity.

The time-resolved confocal fluorescence microscope system (MicroTime 200, Picoquant) was used. A pump laser diode at 485nm (LDH-D-C-485) was set to 26.67 MHz and the pumping beam was focused on the fluorescent protein film via a 50x long distance air objective with a numerical aperture of 0.5. The collected light was initially filtered through a band-pass filter at the central wavelength of 520 nm with a FWHM of 35 nm, and then it was detected via a single-photon avalanche diode (Excelitas). Instrument response function (IRF) is measured by using quenched Erythroisin B. Data analysis were done with reconvolution fits.

We expressed these proteins using the *Escherichia coli (E.coli)* system. The expression and purification of the proteins were done in 6 steps (see Fig. 25a), which were: transformation, induction, cell harvest, lysis, purification and concentration. After eGFP and mCherry were cloned in *E. coli* expression vectors with an N-terminal GST tag, they were transformed into host *E. coli* strains and their expression levels were optimized for increasing the yield by changing growth conditions and expression time. After the

transformed bacteria were grown on plates (see Fig. 25b & 25c) and were induced at large-scale using the optimized conditions, they were harvested and lysed to release their soluble contents that include eGFP and mCherry. GST-tagged fluorescent proteins were then purified using affinity chromatography that makes use of the specific binding between GST and glutathione sepharose beads. Finally, the purified proteins were processed by buffer exchange and concentration after which they were ready for integration onto LEDs.

3.4 Green, Red and White LEDs:

A reservoir with a diameter of 4 mm was prepared to load the protein solutions on the pump LEDs. Transparent silk fibroin proteins were used as a matrix for fluorescent proteins; for this purpose a silk fibroin solution was prepared according to the reference [52] and blended with fluorescent proteins leading to a final concentration of 9 mg/ml. Aliquots of eGFP or mCherry blends were placed into the reservoir and dried at 40 °C for 25 minutes. Sequential layers were generated until the desired color-conversion levels were reached.

The radiant flux density of the LEDs were measured with a FOIS-1 integration sphere (Ocean Optics Inc.; Dunedin, FL) connected to a TORUS-25-OSF spectrophotometer (Ocean Optics Inc.; Dunedin, FL) using OceanView software (Ocean Optics Inc.; Dunedin, FL) for data acquisition. The system was calibrated for radiant flux density using a HL-3-INT-CAL calibrated light source (Ocean Optics Inc.; Dunedin, FL). Photometric values were calculated with ColorCalculator, version 6.03 (OSRAM SYLVANIA, Inc.; Beverly, MA).

3.4.1 Green LEDs

Initially, we integrated fluorescent proteins on LED chips for pure-green and -red color generation, as shown in Figure 27a. The electroluminescence of the LED chip pumps the protein over-coating, and the pump signal was absorbed by the fluorescent proteins, which generate spontaneous emission for pure-color generation. eGFP is an effective fluorophore to convert the blue electroluminescence into green photoluminescence due to its strong optical absorption in blue (see Fig. 27d). By adding eGFP up to 21.8 mg/cm^2 on the blue LED chip we controlled the operating point from pure blue to green color (see Fig. 27b). We observed a slight blue shift (of 4 nm) in the transmitted pump light due to stronger absorption of eGFP in higher wavelengths of the electroluminescence. In contrast to the blue-shift of the pump, we observed a red-shift in fluorescence of the central peak wavelength from 528 nm to 557 nm, which is due to the self-absorption of eGFP. Consequently, we started with a blue pump signal with a (x,y) tristimulus coordinates of (0.13,0.05) and tuned the operating point to a green color of (0.34,0.63). Since the eye sensitivity function has a peak at 555 nm, the luminous efficacy of optical radiation corresponded to a high level of 588 lm/W. The luminous efficiency of the eGFP integrated green LEDs was 11.7 lm/W. In addition, color conversion showed a quasi-linear relation with increasing current bias up to 20 mA of the pump diode without any saturation and a color coordinate change less than 1% under different current injection levels (see Fig. 27c).

3.4.2 Red LEDs

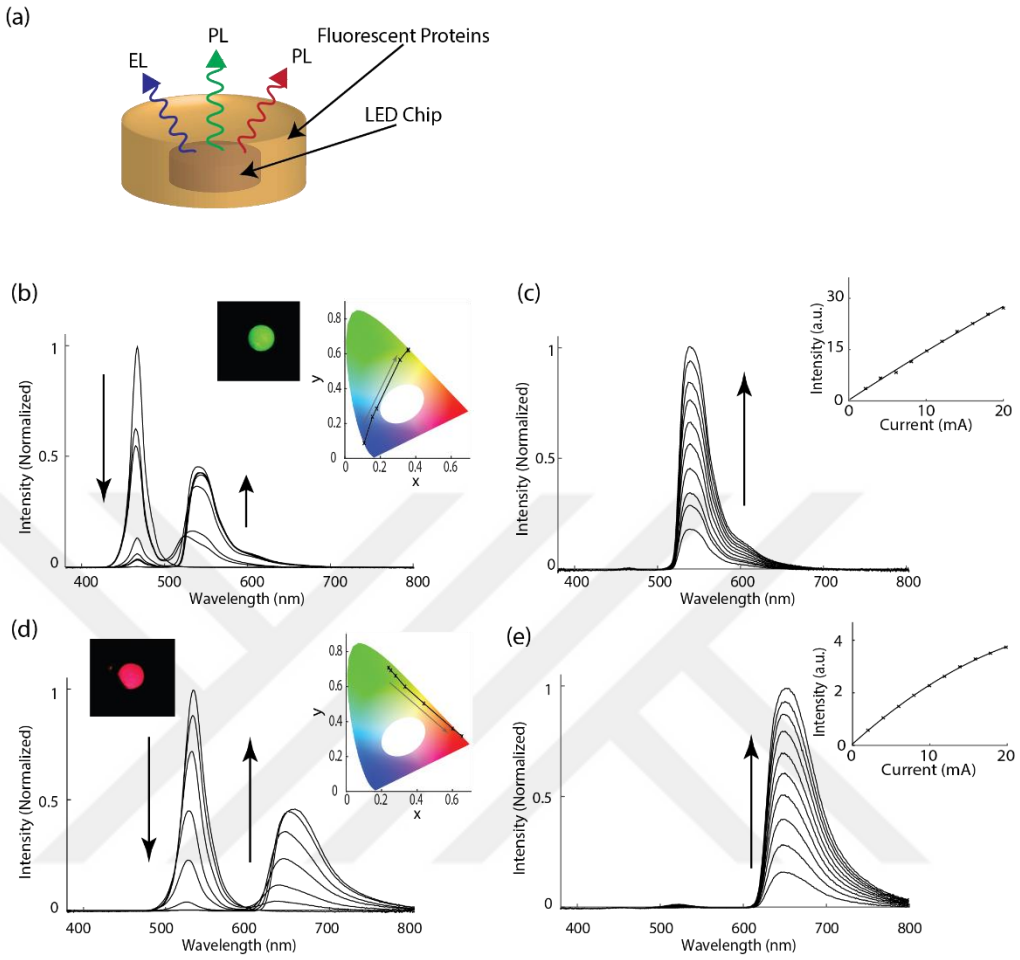

Figure 27. (a) Schematic representation of the fluorescent proteins integrated on LED chips for color conversion. EL and PL refer to electroluminescence and photoluminescence, respectively. (b) The spectra with increasing eGFP amount on blue LED chip. The left inset shows a photograph of the final green color conversion LED. The right inset shows the tristimulus coordinates. From left to right each point corresponds to 0, 2.9, 5.8, 8.7, 11.6, 14.5, 17.5 and 21.8 mg/cm^2 eGFP, respectively. (c) The spectra of the final green color conversion LED with increasing bias current to the blue pump LED from 2-20 mA. The inset shows the intensity vs. current of the color conversion LED. (d) The spectra with increasing mCherry amount on green LED chip. The left inset shows a photograph of the final red color conversion LED. The right inset shows the tristimulus coordinates. From left to right each point corresponds to 0, 1.6, 3.3, 4.9, 6.6, 8.2 and 9.9 mg/cm^2 mCherry, respectively. (e) The spectra of the final red color conversion LED with increasing bias current to the green pump LED from 2-20 mA. The inset shows the intensity vs. current of the color conversion LED.

For red color conversion LED, we integrated mCherry over a green pump LED. Here we used the green LED pump due to its better spectral match with mCherry in comparison with the blue LED pump. The operating points achieved by adding protein up to 9.8 mg/cm^2 over a green pump LED are shown in Figure 27d. We adjusted the tristimulus coordinates from a green color of (0.24, 0.73) to a red color of (0.69, 0.30). We observed a blue-shift (of 10 nm) in the pump signal and a red-shift in the photoluminescence peak from 641 nm to 674 nm. The saturation in photoluminescence intensity with increasing current (see Fig. 27e) is due to the poor electroluminescence of the green pump diode (i.e., "green gap problem") with increasing currents rather than saturation of the fluorophore. (see Fig. 26b)

3.4.3 White LEDs

For white light generation we used the combination of eGFP and mCherry on blue LED chips. Here the electroluminescence of the blue LED pumps the protein over-coating, which generates green and red photoluminescence. The combined emission of the electroluminescence and photoluminescence forms the white light. Today LCD TVs use white light sources as backlight to produce an image on the screen. As an alternative to the current phosphor- and nanocrystal-based backlighting sources, we integrated fluorescent proteins on blue LED chips and used them as a backlight for display application. For this we loaded 5.0 mg/cm^2 of eGFP and 1.4 mg/cm^2 of mCherry, and the spectrum of the LEDs corresponded to a cool white appearance with a correlated color temperature of 8440 K (see Fig. 28a). The protein-integrated backlight exhibited a high luminous efficacy of 248 lm/W. The RGB color coordinates of the backlight were (0.10, 0.17), (0.22, 0.64) and (0.69, 0.31), respectively (see Fig. 28b) and the area of the gamut covers a large portion of the NTSC color space of 80%, which is larger than a yellow phosphor-based color conversion LED of ~68% [53]. By replacing mCherry protein with mPlum on a blue pump at 440 nm, the color gamut could be further expanded, which lead

to a NTSC color space of 114%. We applied the protein-integrated backlight for a 3.5'' LCD TV for the first time, and the colors and objects in the image can be well observed and distinguished, as shown in Figure 28c.

The structure of fluorescent proteins has a direct effect on the generated backlight emission profile. The rigid β-shell in eGFP and mCherry surrounding the chromophore significantly protects quantum efficiency of the protein against static and dynamic quenching mechanisms [54]. The shell hinders the non-fluorescent complex formation that can lead to static quenching. At the same time, the shell also functions as an insulator surrounding the active chromophore and prevents tunneling of the charge carrier wavefunctions to the nearby molecule, which limits the Dexter-type transfer. Therefore, the variation of the spontaneous emission by protein films can be dominantly due to a Förster-type resonant energy transfer (FRET) process. FRET is frequently used in biology as a spectroscopic ruler [55], and it is the non-radiative transfer of an exciton from a higher-energy to a lower-energy state via a dipolar interaction.

Initially, we prepared a fluorescent protein solution in which the average interspacing between the proteins was hundreds of nanometers that is significantly larger than the Förster radius of 5.24 nm between eGFP and mCherry [56]. Since the energy transfer efficiency rapidly attenuates with the interspacing between proteins (i.e., r^{-6}), the possibility of a FRET process diminishes. Thus, the total decay rate (k) will solely depend on the radiative and non-radiative recombination rate of proteins (k_R and k_{NR}, respectively), as shown in eq. 1. The total decay rate of eGFP emission was 0.130 ns^{-1} (see Fig. 28d).

$$k = k_R + k_{NR} \quad (1)$$

We investigated the FRET dynamics of the protein film on a LED chip for display backlight. Since the eGFP and mCherry blend were dried on a LED chip, the proteins were in close proximity. Thus, in addition to the interband radiative and non-radiative recombination rate, an additional decay channel appears due to the donation of energy

absorbed by eGFP to the nearby mCherry (k_{FRET}) (see equation 2). Therefore, the total decay rate of the eGFP increased to 0.179 ns^{-1}, which corresponds to a FRET rate of 0.049 ns^{-1} with a FRET efficiency (η) of 0.273 (see equation 3). Therefore, red color conversion was improved by transferring the energy non-radiatively from the eGFP donor to the mCherry acceptor via FRET.

$$k = k_R + k_{NR} + k_{FRET} \quad (2)$$

$$\eta = \frac{k_{ET}}{k_{ET} + k_{NR} + k_R} \quad (3)$$

In addition to the FRET process, the red color conversion was further amplified with the increased confinement of light in close-packed film due to the increased refractive index mismatch in comparison with the solution based color conversion (from $\Delta n_{solution}=n_{water}-n_{air}= 0.33$ to $\Delta n_{dry}=n_{protein}-n_{air}= 0.51$ [49]). The increased refractive index mismatch leads to an increased absorption path of mCherry for eGFP emission. Therefore, color-conversion of red was enhanced by 1.8-fold at steady-state (see Figure 28e), which is beyond the FRET process. Moreover, the delayed rise in the time-resolved emission of protein film originates from the homo-transfer and contributes to the widening of the emission spectrum.

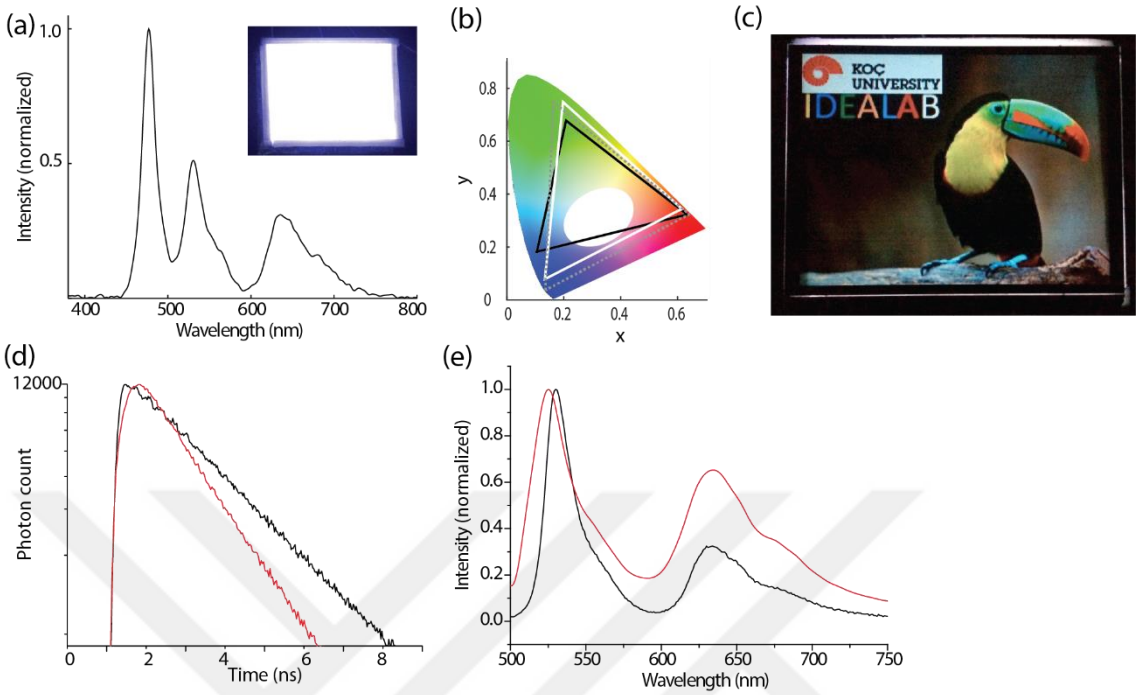

Figure 28. (a) The spectrum and photograph (in the inset) of fluorescent protein integrated backlight after the diffuser part of the LCD TV. (b) The color gamut triangle of the backlight (black), the theoretical backlight (grey) using a 440 nm pump LED, eGFP and mPlum proteins, and the NTSC color space (white). (c) A photograph of a 3.5'' LCD display image illuminated via fluorescent protein integrated backlight. (d) Time-resolved spectroscopy and (e) fluorescence of in-film (red) and in-solution (black) eGFP and mCherry blends.

3.5 WLEDs for displays

Two white LEDs were placed at the base of a box with a diffusor and a 3.5" TFT screen placed on top. Images were uploaded onto the screen with a LaCinema Classic Mediaplayer (LaCie; Paris, France).

3.6 Fluorescent protein integrated white LEDs for general lighting

Table 6 The table summarizes the structural and photometric properties of fluorescent protein integrated white LEDs.

	Light type	**Density of eGFP (mg/cm^2)**	**Density of mCherry (mg/cm^2)**	**x**	**y**	**CCT (K)**	**CRI**	**LE (lm/W)**	**LER (lm/W)**
WLED 1	Warm	13.1	3.3	0.39	0.38	3721	42	1.9	202
WLED 2	Daylight	9.7	0.8	0.36	0.41	4601	66	3.3	266
WLED 3	Cool	6.1	0.4	0.26	0.36	8577	83	6.7	291

The color temperature of white light sources plays a central role in their recommended uses. Here we demonstrated fluorescent protein integrated cool, daylight and warm white LEDs that fit for a variety of applications in general lighting. Initially we integrated 13.1 mg/cm^2 eGFP and 3.2 mg/cm^2 mCherry as sequential color conversion layers on a blue LED chip (see Table 6). The generated white light corresponded to a warm-white appearance with a correlated color temperature (CCT) of 3721 K (see WLED1 in Figure 28a). The red-emitting mCherry balanced the fluorescence of the green-emitting eGFP and the electroluminescence of the blue LED. Thus, the chromaticity coordinates remained inside the white region of the CIE chromaticity diagram. Moreover, WLED1 showed a color rendering index of 42 and a luminous efficacy of optical radiation of 202 lm/W. The luminous efficacy of the optical radiation was relatively low because the LED spectrum contains a significant emission above 650 nm where the eye sensitivity is weak. In addition, since the quantum efficiency of mCherry is relatively low (0.22) and is further reduced while integrated as a protein film, this led to a luminous efficiency of 1.9 lm/W for WLED1.

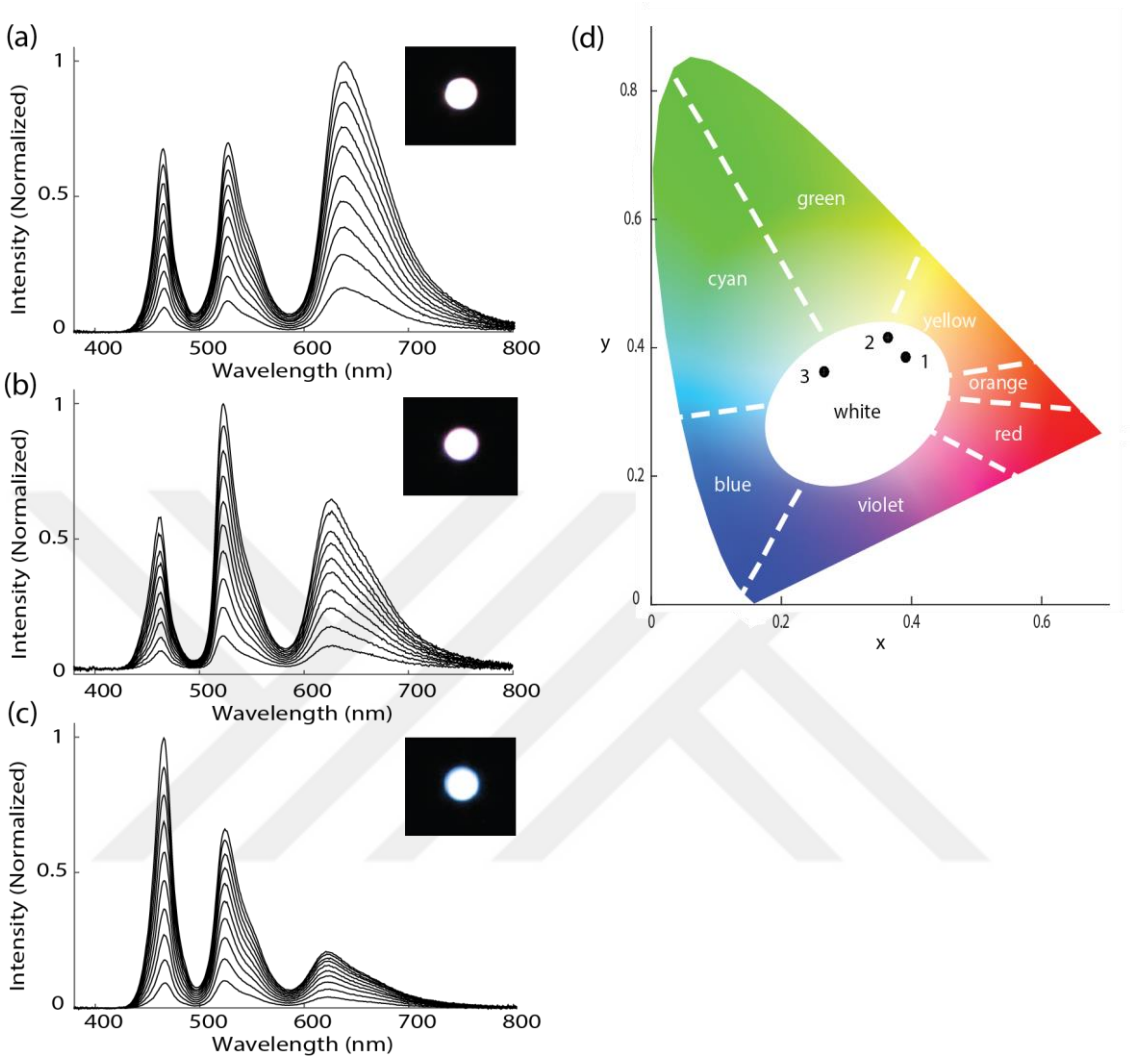

Figure 29. The emission spectra of fluorescent protein integrated (a) warm-, (b) daylight- and (c) cool-white LEDs at increasing current injection levels from 2 to 20 mA (denoted as WLED1, WLED2 and WLED3, respectively). The insets of each figure show the photograph of the white LEDs. (d) The chromaticity coordinates of WLED1, WLED2 and WLED3.

Next we tuned the color temperature to cooler regions and for this we relatively decreased the eGFP and mCherry content of the color conversion layer to 9.6 and 0.8 mg/cm^2, respectively (WLED2). WLED2 showed a daylight white appearance (see Fig. 28b) with a CCT of 4601 K and an increased luminous efficacy of optical radiation of 266 lm/W. The reduced amount of mCherry resulted in less color conversion in red, and the decrease

in eGFP increased the transmission of blue pump light, while decreasing the eGFP photoluminescence and consequently mCherry photoluminescence. Furthermore, this WLED exhibited an enhanced luminous efficiency of 3.34 lm/W and a color rendering index of 66.

For the third white LED (see WLED3 in Fig. 28c) we further decreased the green and red spectral content by reducing eGFP and mCherry to 6.0 and 0.4 mg/cm^2, respectively, and thus shifted the operating point to a cool white appearance with a CCT of 8577 K. Today cool white LEDs are also used for external lighting application due to the Purkinje shift of the eye sensitivity function toward blue in circumstances with low light intensity levels [57]. The luminous efficacy of optical radiation was increased to 291 lm/W because the intensity at deep-red wavelengths was low. In addition, since the transmitted blue electroluminescence was relatively high, this led to an increased luminous efficiency of 6.7 lm/W. WLED3 excels in color-rendering with a CRI of 83, which is higher than a conventional white LED made of yellow phosphor [31]. Our theoretical calculations suggest that the addition of a yellow fluorescent protein could further lead to a color rendering index of above 90 (see the white LED spectrum in Figure 30).

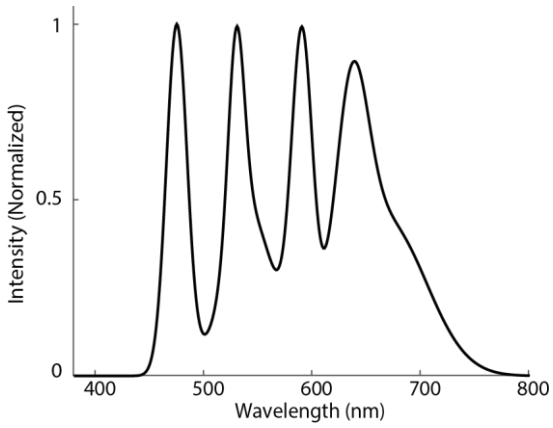

Figure 30. A theoretical spectrum generated by adding a yellow fluorescent protein to the eGFP and mCherry emission on blue LED chip. This spectrum shows a correlated color temperature of 3810, color rendering index of 90, luminous efficacy of optical radiation of 283 lm/W and chromaticity coordinates of x=0.39 and y=0.41.

3.7 Conclusion

Since their discovery in the 1960s, fluorescent proteins (FPs) have become an integral tool in molecular and cell biology, and recently these versatile molecules are finding interesting applications in photonics, for example, in biological cell lasers and solid-state lasers [54, 58, 59]. Fluorescent proteins provide a green material that can be safely used for device applications. The expression of the fluorescent proteins using bacterial expression systems allows for sustainable and large-scale production that can lead to highly abundant and low cost material. Advantageously, the production of these materials does not require high processing temperatures and thus they have low embodied energy. Moreover, the proteomic nature of these fluorescent emitters are biocompatible and have been expressed in the tissue of the living animals such as zebra fish and mice [60, 61]. They provide a safer material for lighting applications in comparison with nanomaterials [62]. In general, equipment (e.g., TVs, mobile phones, etc.) is replaced with their newer version before the end of their functional lifetime; the transient materials (e.g., proteins) that can safely degrade in nature can be beneficial for disposal and waste management.

Today there are more than 50 types of fluorescent proteins that can be directly used for technological applications [63]. If we look at the progress in colloidal semiconductor nanocrystals, first the core materials were demonstrated with low quantum efficiency [64], and then their stability and efficiency were enhanced with the development of core-shell type structures [65]. The naturally-occurring nanostructure of fluorescent proteins has converged to a core-shell type structure that has the emitting part of the molecule protected by a barrel-shaped shield. In addition, there is significant room for development of novel proteins with enhanced brightness and photostability [66], which can significantly improve the device performances.

Chapter 4 Silk Hydrogel Lenses

In this chapter we demonstrate silk hydrogel lenses for LEDs. First of all, silk fibroin solution preparation and its transformation to hydrogel procedure is mentioned. Dome and crater lenses prepared using molds and silk hydrogel transmittance, radiation pattern and light extraction efficiency is analyzed for different concentration of silk fibroin solution.

4.1 Introduction

LED chips are made of semiconductor die, wire bond, heat sink, metal contacts, package and lens [25]. In this structure, lenses are used to enhance efficiency, modify the viewing angle and pattern the generated light. Lenses are fabricated from mostly silicone based polymers, epoxy resin and poly methyl methacrylate (PMMA), and the environmental compatibility is mostly unknown and even can be hazardous for environment [67]. In the LED chip lenses occupy significant portion of the whole device. Hence, in conjunction with the estimated increasing LED production, transition of LED lenses based on eco-friendly materials is significant for sustainable and clean environment [68]. For this reason, in this part of the thesis we made eco-friendly lenses using silk fibroin hydrogels.

Hydrogels are widely used in tissue engineering, scaffold, cell based sensing and optogenetics [69, 70]. Mainly, silicone hydrogels were used for fabrication of contact lens [71-75]. Silk fibroin which was obtained from Bombyx-mori cocoons is a special material for biomedical applications [2, 76-78] and recently, a new type of silk hydrogel was produced which featured elastomeric and tunable mechanical and degradation properties [75, 79, 80].

In this study, silk hydrogel was used as a lens for collimating and dispersing light coming from LEDs. Transmittance, light extraction efficiency and intensity distribution of spatial radiation of silk hydrogels were investigated. Crater-type and dome-type lenses were designed and their silk hydrogel lenses are prepared using molds. Measurements of intensity distribution of spatial radiation matched the simulated results and revealed optimal extraction efficiency for 8wt% silk hydrogels.

4.1 Silk Fibroin

Silk fibroin is a natural protein and directly extracted from silk cocoons produced by Bombyx mori silkworm. Therefore, it presents a "green" material for photonic applications with its advantageous properties of biocompatibility and high optical transparency with a minimal absorption. Combining these properties with high thermal performance makes this biomaterial promising for future optoelectronic applications. Silk solution preparation takes at least 3 days as shown in the figure 31. It consist of 3 major steps.

1. Fibroin extraction
2. Dissolving silk fibroin
3. Dialysis and centrifugation

Figure 31 ***Silk solution preparation steps***

4.1.1 Fibroin extraction.

Silk cocoons consist of fibroin and surrounding sericin as it is observed in Fig. 32. In fibroin extraction step our aim is to remove sericin by that way extract fibroin.

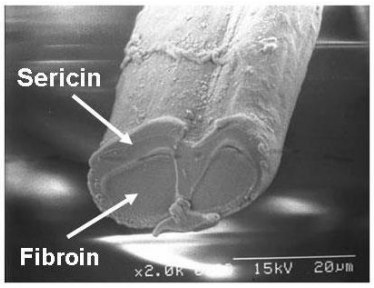

Figure 32. Fibroin SEM [81]

Step 1: Prepare and heat 2-liter glass beaker filled with deionized water.

NOTE: Before starting next steps involving step 1 water must be boiling or else sericin will not be fully removed from water.

Step 2: Cut cocoons with scissors and dispose the silkworm. It is better to cut them into small pieces. Measure 5 g.

Figure 33. Cocoons and silkworm

Step 3: Weight 4.24g of Sodium carbonate

Step 4: Add 4.24g sodium carbonate in the boiling water and stir it. The molarity of obtained solution is 0.02M.

NOTE: Even of the amount of silk is varied between 5g and 20g the molarity of solution and amount of sodium carbonate should remain constant.

Step 5: Add 5g cocoons into boiling Sodium carbonate solution. Boil for 30 mins.

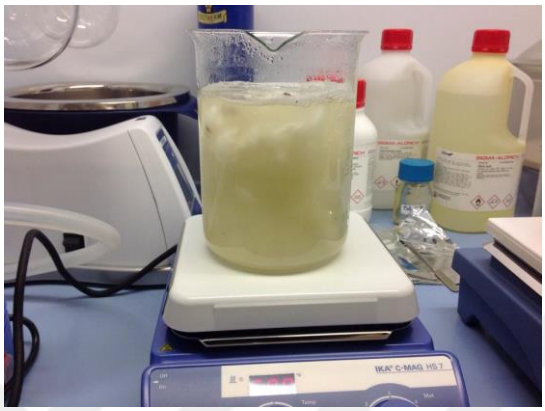

Figure 34. Silk cocoons boiling in hot water

Step 6: Remove the silk fibroin and rinse in cold deionized water. Be careful the silk fibroin will be hot.

Step 7: Place the silk fibroin in 1 liter pure water and rinse the silk fibroin in deionized water for 20 min and stir. Repeat this procedure twice.

Figure 35. Rinse in pure water.

Step 8: Remove silk and squeeze it. Allow it to dry overnight.

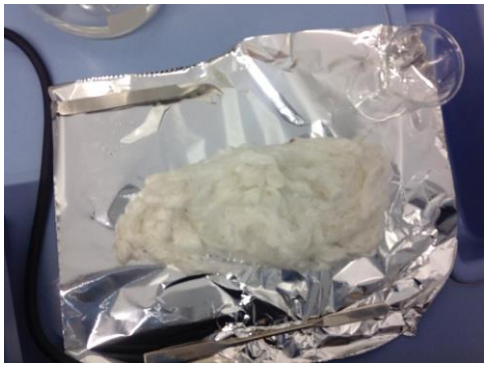

Figure 36. Degummed silk fibroin

NOTE: Degummed silk fibroin can be stored at room temperature indefinitely.

4.1.2 Dissolving silk fibroin

The aim of this procedure is to make silk fibroin transparent. Its tertiary structure of silk fibroin makes it not transparent. We introduce LiBr to break Hydrogen bonding thus destroying tertiary structure. In this way the silk fibroin will be transparent.

Step 1: Weigh degummed silk fibroin (X). 20% (wt/vol) LiBr solution should be prepared.

$$\left(86{,}65\frac{g}{mol}\right)\left(9{,}3\frac{mol}{l}\right)\left(\frac{1l}{1000ml}\right)(4X) = \_\_\_\_\_\ g\ of\ LiBr$$

NOTE: Mixing LiBr with water is exothermic process; hence, lot of heat will be produced. Doing this step on ice is suggested.

Figure 37. Silk fibroin mixed with LiBr

Step 2: Mix 9.3M LiBr solution with silk fibroin and place in the oven at 60 C for 4 hours.

Figure 38. Dissolved silk fibroin.

4.1.3 Dialysis and centrifugation

The aim of this procedure is to remove the LiBr from dissolved silk solution then centrifuge it to get rid of other impurities like remaining silk worm particles.

Step 1: 12ml 3.5KMW dialysis cassettes are used. Hydrate dialysis cassettes.

Step 2: With 20 ml syringe and 18 gauge needle insert 12 ml dissolved silk solution into the dialysis cassette.

NOTE: 21 guage(standart) needles are not recommended. Viscosity of silk solution makes it to hard to go through needle.

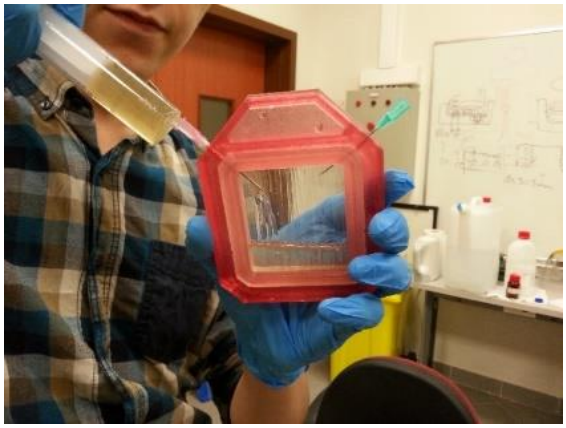

Figure 39. Dialysis cassette

Step 3: Dialyze against 1 liter pure water. Use stir bars for the whole procedure. Change water after 1h, 4h, midnight, morning, midnight and morning.

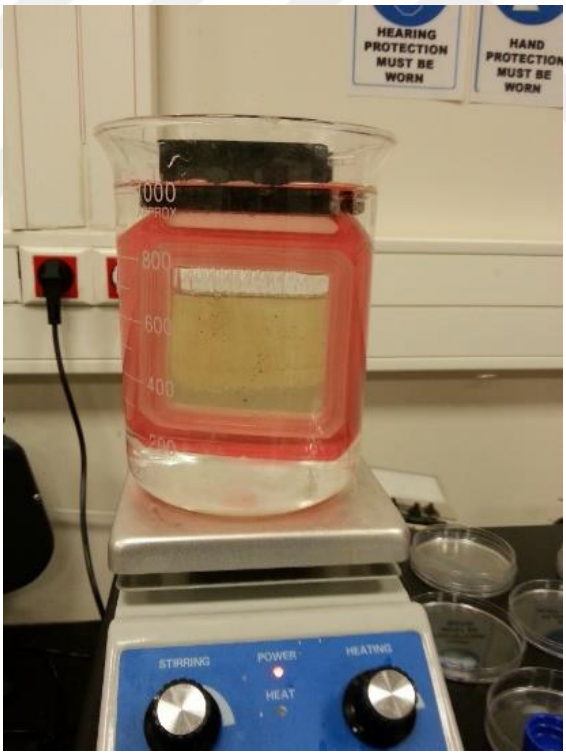

Figure 40. Dialysis process

Step 4: Remove silk solution from dialysis cassette.

Step 5: Centrifuge at 9000 rpm for 20 mins at -2C two times.

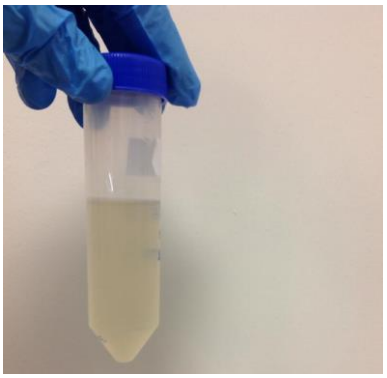

Figure 41. Silk solution

4.2 Transmittance of silk hydrogels

Silk solution preparation was carried out according to the reference [52] as follows: 5 g cocoons cut in half were disposed of the worms and boiled in 2 L, 0.02 M Na_2CO_3 (Sigma-Aldrich, St. Louis, MO) solution for 30 mins to remove gum like sericin. Then, degummed cocoons were rinsed twice for 20 min in 1 L deionized water under continuous stirring and dried in air. Dried degummed cocoons were mixed with 9.3 M LiBr (Sigma-Aldrich) solution (1 g /4 ml) and kept in oven at 60^{o}C for 4 h. Dissolved silk were dialyzed with dialysis cassettes (3500 MWCO, Thermo Scientific) against 1 L deionized water for 2 days under continuous stirring to remove LiBr. Water was changed periodically at 1, 4, 12, 24 and 36 h. Finally, the silk solution was centrifuged at 9000 rpm for 20 min at -2 ^{0}C twice to remove impurities. The obtained silk solutions were 8-10 wt% in water. To obtain higher concentration of silk solution, 15 ml of 8-10 wt% silk solution was concentrated in oven for 4 h, at 60°C. By thermal concentration, we achived silk solution concentration of up to 28 wt%.

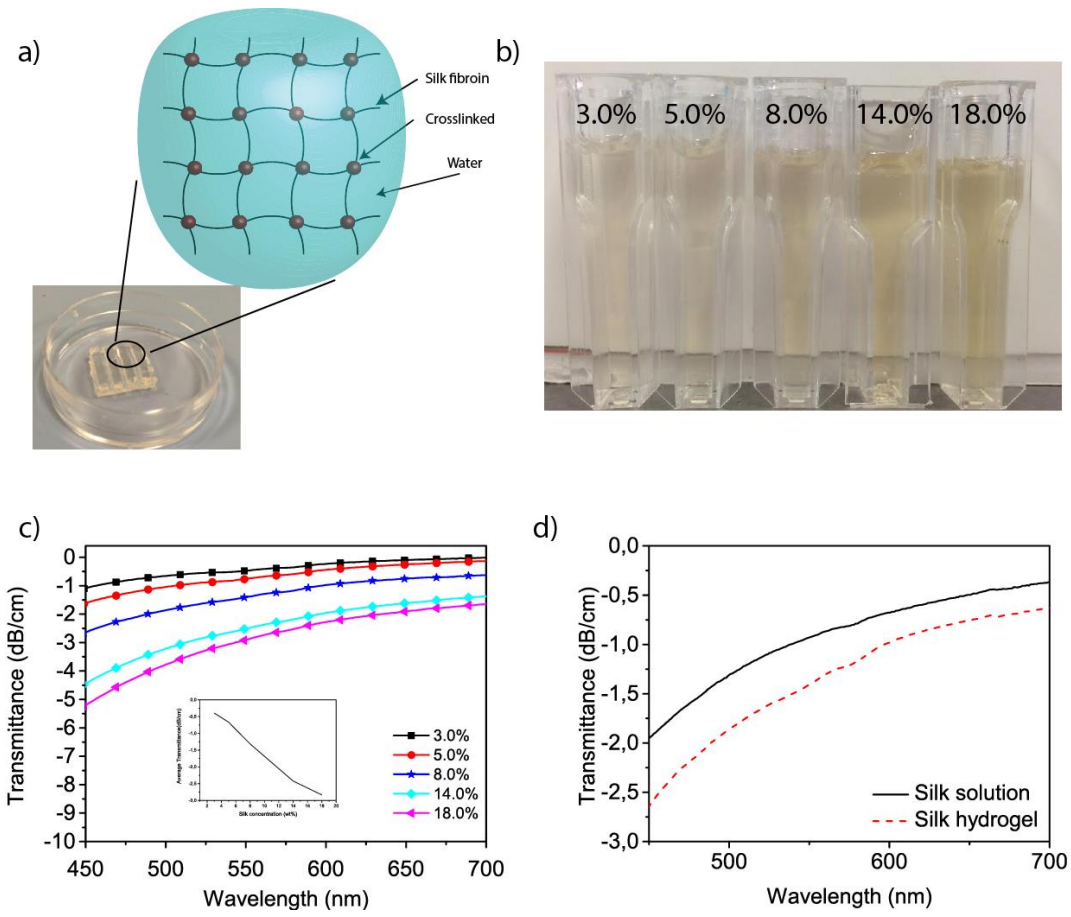

Figure 42. ***Silk hydrogel.*** *a) Silk hydrogel structure schematic. Water molecules are trapped inside covalently crosslinked tyrosine residues in silk fibroin solution b) Photograph of silk hydrogels in cuvette with 3, 5, 8, 14 and 18 wt%. c) Transmittance of silk hydrogels in dB/cm units in visible spectrum for 3, 5, 8, 14 and 18 wt%. d) Comparison of silk solution transmittance and silk hydrogel transmittance for 8 wt%.*

Silk hydrogels were prepared by covalently bonding tyrosine residues in silk solution (see Fig 42a). For that 1000 U/ml stock type VI horseradish peroxidase (HRP) (Sigma-Aldrich) solution were prepared by mixing 4 mg of HRP with 1 ml deionized water [79]. Silk hydrogels were prepared by adding 10 U of HRP to 1 ml of silk solution. After sonication 10 µl of 1% H_2O_2 was added to 1ml of silk HRP solution [82]. In 20 mins, silk hydrogels were formed.

The optical transparency of materials is important parameter for light guiding and extraction applications in optoelectronics devices. We tune the transmittance of the silk hydrogels by using various concentration. We investigated the transmittance of silk fibroin with the concentration of 3.0, 5.0, 8.0, 14.0, 18.0 wt% (see Fig. 42 b) and we measured their transmittance spectra (Fig. 42c). Higher concentration of silk hydrogel exhibits relatively lower transmittance of silk hydrogel (0.17 (dB/cm)/wt% decrease) (see Fig 42.c inset). Visibly, as the fibroin protein concentration increases, the silk hydrogels start to show a yellowish appearance due to high attenuation in shorter wavelengths (see Fig. 42b). According to the measurements of transmittance for various hydrogels, the attenuation was strongly dependent on silk concentration. For example, the hydrogel with 18 wt% silk solution shows -2.9 dB loss per cm at 550 nm (see Fig. 42c), but as we decrease the protein content in the hydrogel, the transmittance increases to -0.5 dB per cm at 550 nm for 3 wt% silk solution. Since the absorption of water is comparatively small (e.g., 0.0003 dB/cm at 550 nm [83]), the loss of light in these hydrogels dominantly comes from the silk proteins. We aimed to understand the effects of crosslinking on the transmittance while the fibroin proteins are crosslinked with HRP and hydrogen peroxide and the structure of the solution turns into hydrogel. For this purpose we explored the effect of transition from solution to hydrogel on optical transmittance by measuring it in both fibroin solution and hydrogel forms (see Fig 42d). The decrease in transmittance between 450-7700 nm is 0.41 db/cm. Therefore, we can conclude that the crosslinker has a relatively small effect on transmittance of silk hydrogel in comparison with silk fibroin.

4.3 Radiation pattern

A useful advantage of using hydrogels is that they can be molded in any shape as suited for specific application [70, 84-86]. To shape the silk solutions to make LED lens, we have used molds designed with Solidworks software and 3D printed with ULTRA

3SP.The silk solutions were poured in these molds and afterwards covalently crosslinked [79]. Lenses are generally utilized to manipulate the light to collimation or dispersion. To demonstrate silk hydrogel adaptability for collimation and dispersion we fabricated crater and dome by molding (see Fig. 42a) [2].

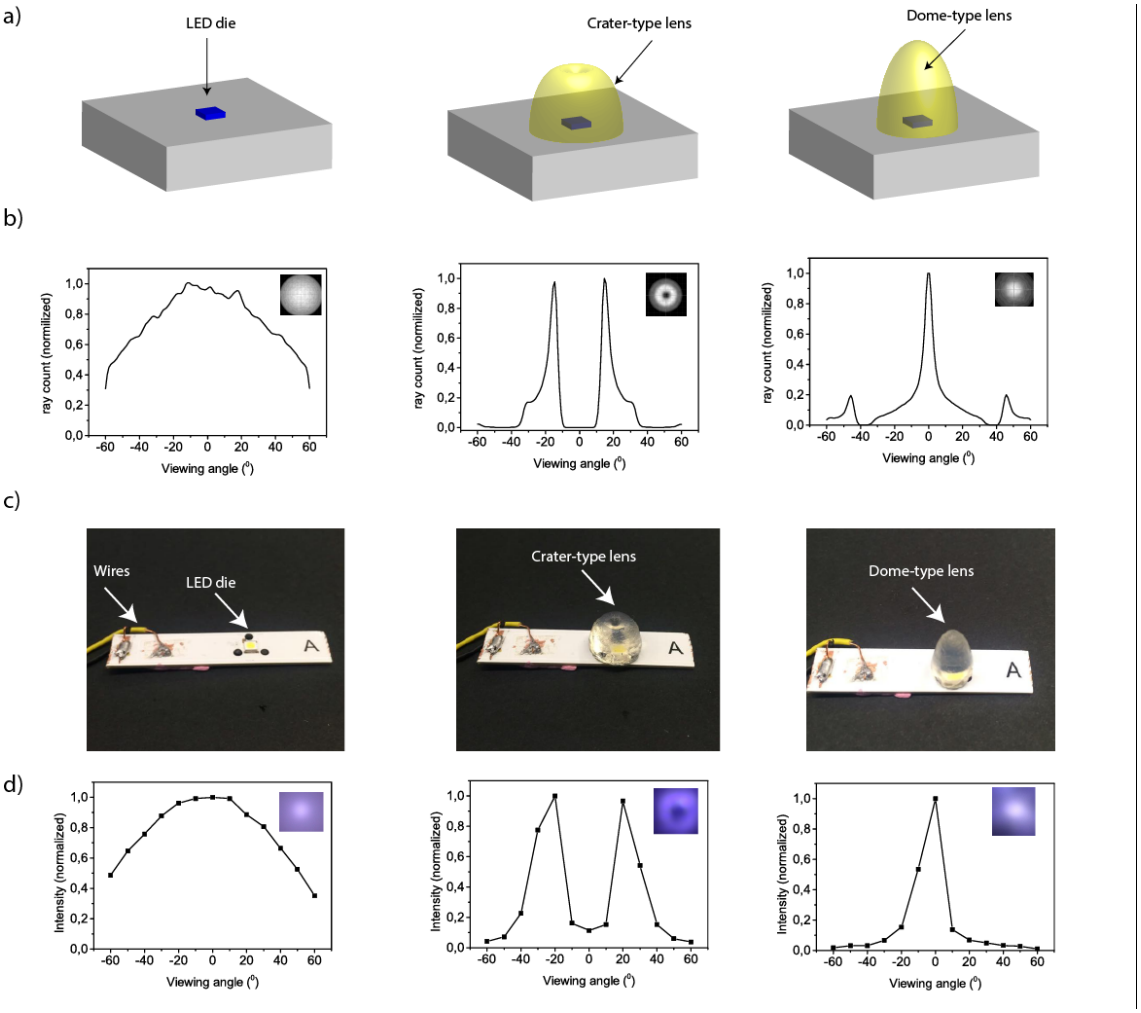

Figure 43. ***Intensity distribution of spatial radiation.*** *a) Three dimensional model of WLED chip (left), crater-type lens on WLED chip (middle) and dome-type lens on WLED chip (lens). b) Ray tracing simulation results of WLED chip (left), crater-type lens on WLED chip (middle) and dome-type lens on WLED chip (lens). c) Photographs of WLED chip (left), crater-type silk hydrogel lens on WLED chip (middle) and dome-type silk hydrogel lens on WLED chip (lens). d) Experimental results of WLED chip (left), crater-type silk hydrogel lens on WLED chip (middle) and dome-type silk hydrogel lens on WLED chip (lens).*

The intensity distribution of light in space shows the radiation pattern of lenses [2]. To investigate the radiation pattern, we used ray tracing method. As the reference LED emission without lens we measured the radiation pattern of the sole LED die that shows uniform spatial profile and Gaussian angular profile with half angle of 90º in X and Y coordinates. Then, we generated an identical LED die emission profile in ray tracing software. To understand the effect of lenses on light distribution profile, the crater-type and dome-type lenses were simulated on top of the LED die. Numerical simulation of ray tracing on WLED chip with and without lens is shown in Fig. 2b. The crater-type lens (see Fig. 43b, middle) exhibits maximum intensity of light at 20^0 and -20^0 which disperse light to wider angles. In contrast, dome-type lens (see Fig. 43b, right) shows focusing.

Intensity distribution of spatial radiation of blank white light emitting diode (WLED) (LG Innotek LED BLU, without lens), crater-type silk hydrogel lens and dome-type silk hydrogel lens on WLED were measured (see Fig. 43c) and experimental measurements and numerical simulations shows good correlation. The Crater-type lens shows maximum intensity of light at 16^0 and -16^0, which is close to the value of numerical simulations and the dome-type lens shows similar collimation of light around the center. However, scattering properties of the silk hydrogel contributes to the broadening of the peaks in crater- and dome- type silk hydrogel lenses.

4.4 Light extraction efficiency

Light extraction efficiency of lens can influence the efficiency of LEDs [87]. To analyze the extraction, we made silk hydrogel hemisphere lenses with 3, 5, 8.2, 14, 28 wt% silk solutions at a diameter of 7 mm were prepared and placed into integrated sphere (Ocean Optics, FOIS-1). A spectrophotometer (Ocean Optics, Torus) connected integrating sphere and HL-3 VIS-NIR light source (Ocean Optics, HL-3 VIS-NIR) were used to measure the light extraction efficiency of the prepared samples using the optical setup in

Fig 44a. As a control experiments, reference light intensity was measured for integrating sphere without any lens. Silk hydrogel lenses were placed in integrating sphere and the resulting intensity was measured. The resultant spectrum contains all scattering light and backscattered light contribution was assumed as negligible. We analyzed the extraction efficiency at all concentrations (see Fig. 44c). We found that the light extraction efficiency decreases with concentration of silk hydrogel (see Fig. 44b). In Fig. 44c light extraction efficiency is shown in the visible spectrum. From UV-Vis transmittance and light extraction efficiency plots it can be concluded that scattering has significant contribution for decrease in transmittance.

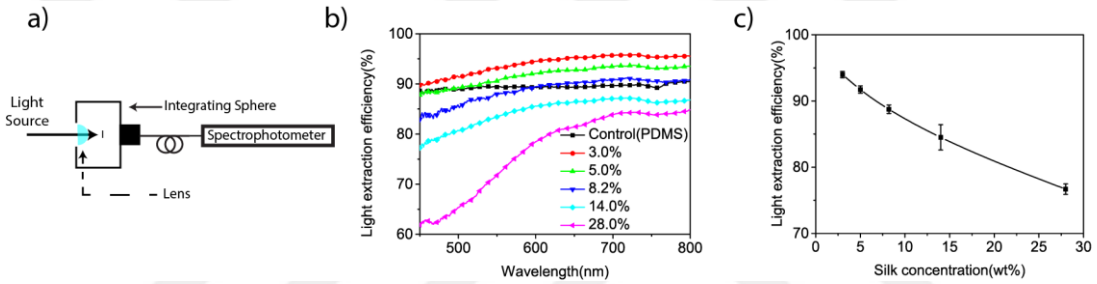

Figure 44. ***Light extraction efficiency*** *a) Optical setup to measure light extraction efficiency. b) Light extraction efficiency of silk hydrogel lens with 3.0, 5.0, 8.2, 14.0 and 28.0 wt% over visible spectrum with control lens (PDMS). b) Average light extraction efficiency of silk hydrogel lens.*

We compared the performance of the silk hydrogel with other lens encapsulant materials. Silk hydrogel lenses with low concentration have better light extraction efficiency than control (PDMS) lens. 3 wt% silk concentration hydrogel had the highest light extraction efficiency of 94%.

The degradation (see Fig. 45) of silk hydrogel lenses is also a very important parameter for specific surgical applications [88]. For example, endoscopes use cameras and LEDs on tips of apparatus that are inserted inside a human body for easy view of areas of treatment. These Camera and LEDs are usually covered with lenses. Using wireless technology these devices covered in silk hydrogel lens could be monitored inside human

body. Moreover, due to 90% water content in hydrogels these lenses could be integrated with underwater LEDs.

Degradation of silk hydrogels can be significantly slowed down with polymer coating to reduce water content evaporating [89].

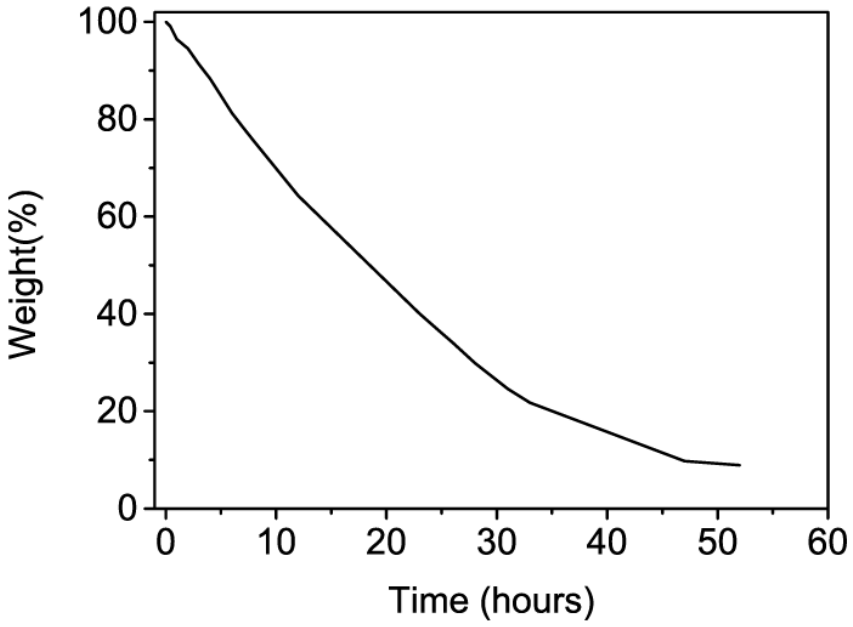

Figure 45. Degradation of 8.4 wt% silk hydrogel

Chapter 5 Conclusion

SSL has potential to replace conventional lighting in near future due to higher efficiency, long lifetime and small size, because of high demand for SSL in near future, massive amount of waste that will be generated can be lowered by the use of eco-friendly materials. FP and silk fibroin are one of these materials where their optoelectronic properties can be beneficial to decrease the e-waste due to LEDs. In this study we combined SSL, FP and silk fibroin and made eco-friendly WLEDs. We aimed to make high CRI WLEDs where their radiation pattern can be controlled with silk hydrogel lenses.

We proposed the idea of using fluorescent proteins for color-conversion LED applications in 2013 and this proposal get accepted by the Marie Curie Actions (with the project acronym PROTEINLED and number 631679) and started the project in 2014. In the same year, we also applied a patent for these LEDs. In 2016, we demonstrated the first use of fluorescent proteins for display applications.

We calculated theoretical maximum achievable CRI values for single, double and triple combinations of FPs using MATLAB. It was assumed that self-absorption shifts only the peak of the emission spectra, thus the shape of the spectra doesn't change. For single color conversion maximum achievable CRI was 76, to improve we added one more FP and CRI increased to 94 which was sufficiently enough however to reach the limits three FP were used in the simulation. The resulting CRI was 98 which was first-rate.

Moreover, we demonstrated light emitting diodes integrated with biologically-derived fluorescent proteins. We showed the use of fluorescent proteins starting from the bacterial expression to their application in general lighting and displays. Their eco-friendly properties of low embodied energy, biocompatibility and biodegradability combined with the tunable color-properties and high quantum yield make them a strong candidate for

photonic devices. The combinations of different protein emitters enables sensitive tuning of photometric properties for application-specific lighting sources. Fluorescent proteins show promise for efficient and high-quality lighting. The development of novel fluorescent proteins will further improve the efficiency levels and extend the color gamut. Therefore, there is plenty of room in fluorescent protein design, engineering and integration for device applications.

We introduced silk hydrogel as an optical material for lens application. We fabricated crater- and dome-type lenses from silk hydrogel and showed that the lenses can focus or disperse light from the LEDs. We optimized the transmittance and extraction efficiency of the lenses by tuning the concertation of the silk hydrogel and for 3 wt% silk hydrogel lens 94% light extraction efficiency was attained. We also complimented experimental observation with simulations. From our experimental results, we believe that silk hydrogel is promising bio-friendly alternative be used as a lens in light emitting diodes.

In summary, in this thesis the green material of fluorescent and silk fibroin proteins were used as a color conversion layer and lenses to control the radiation pattern, respectively. We believe that these green materials can find use in future-solid state lighting sources.

Appendix

Appendix 1. FPs emission and absorption spectra

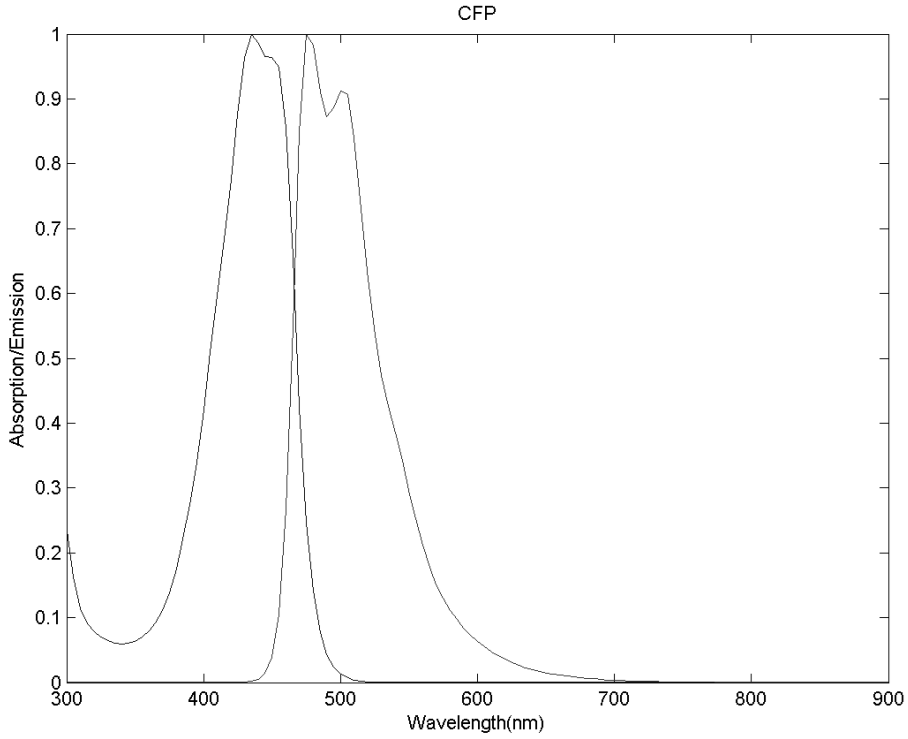

Figure 46. CFP absorption and emission spectra

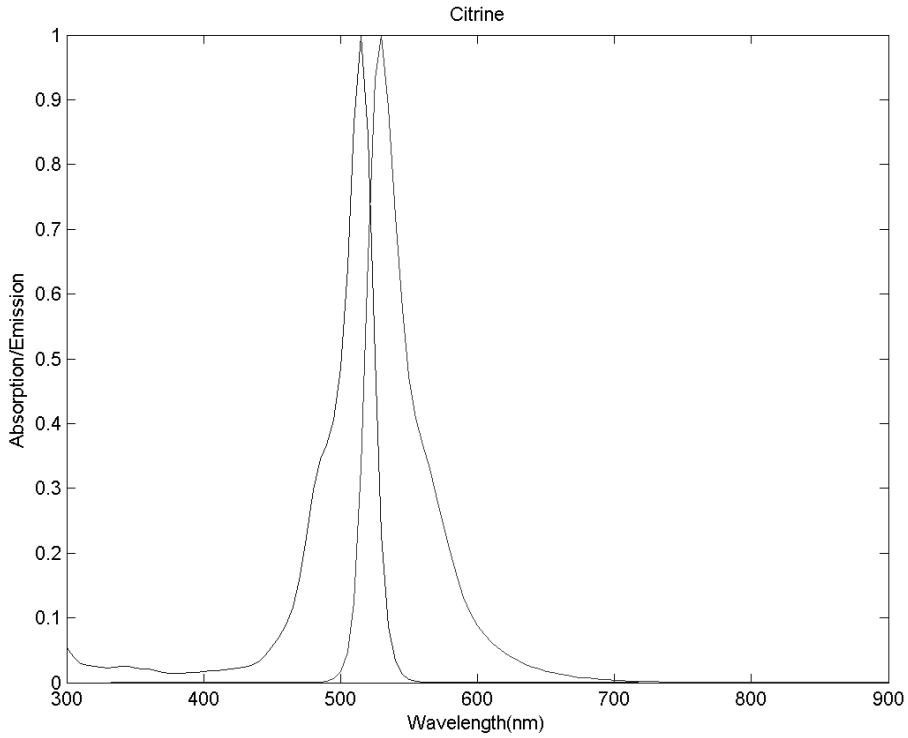

Figure 47. Citrine absorption and emission spectra

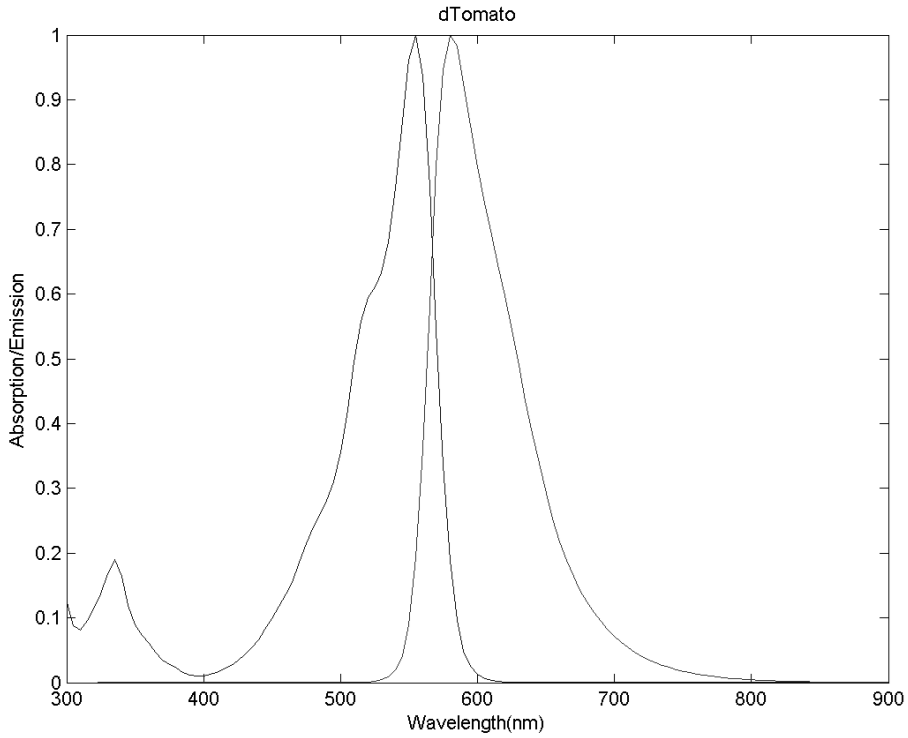

Figure 48. dTomato absorption and emission spectra

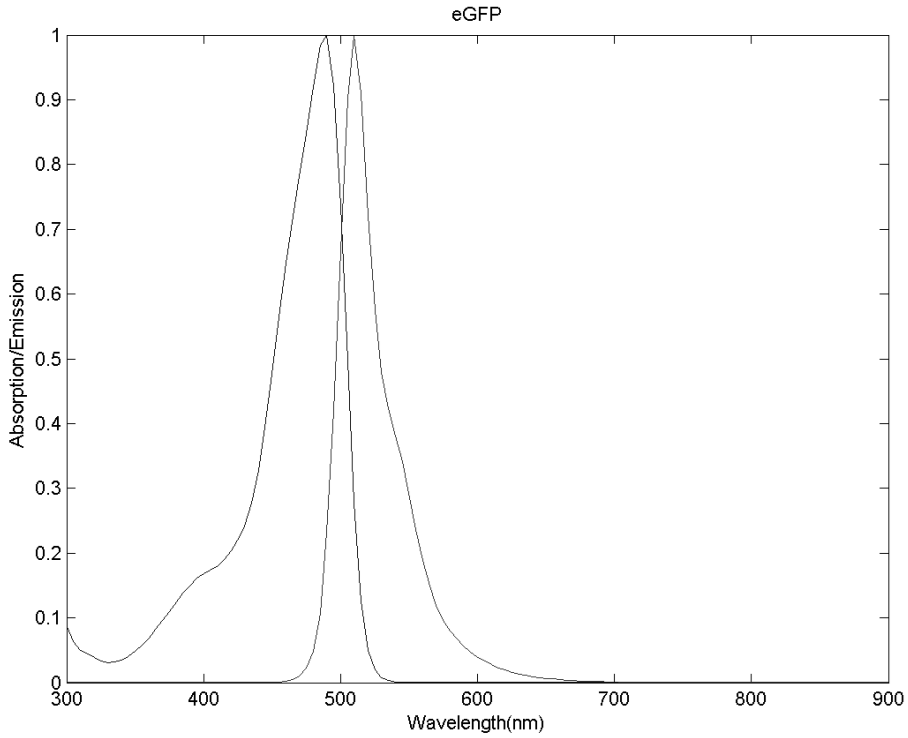

Figure 49. eGFP absorption and emission spectra

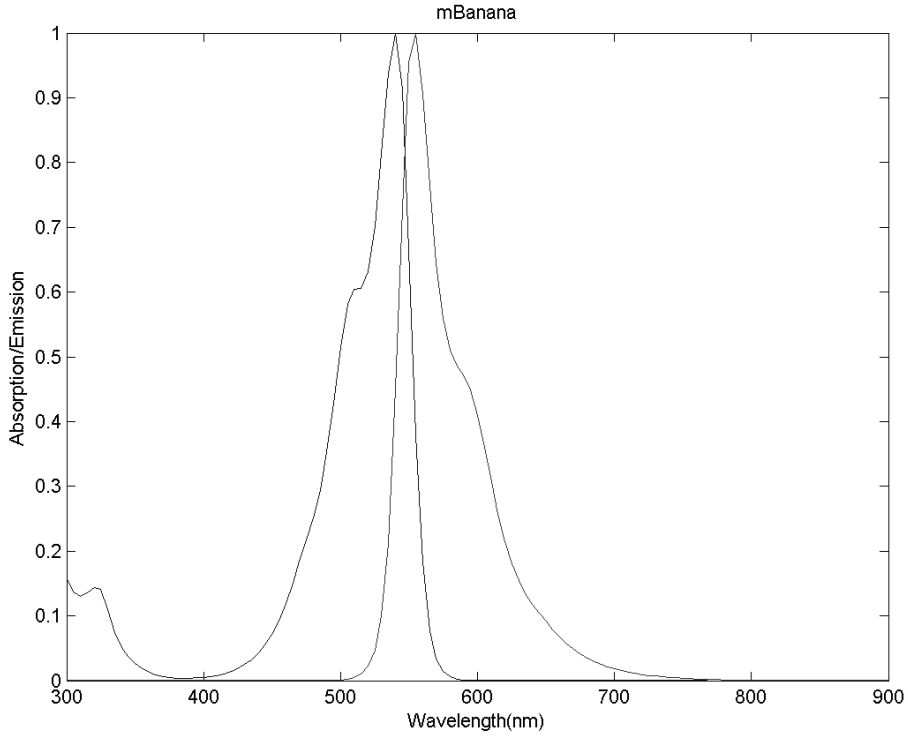

Figure 50. mBanana absorption and emission spectra

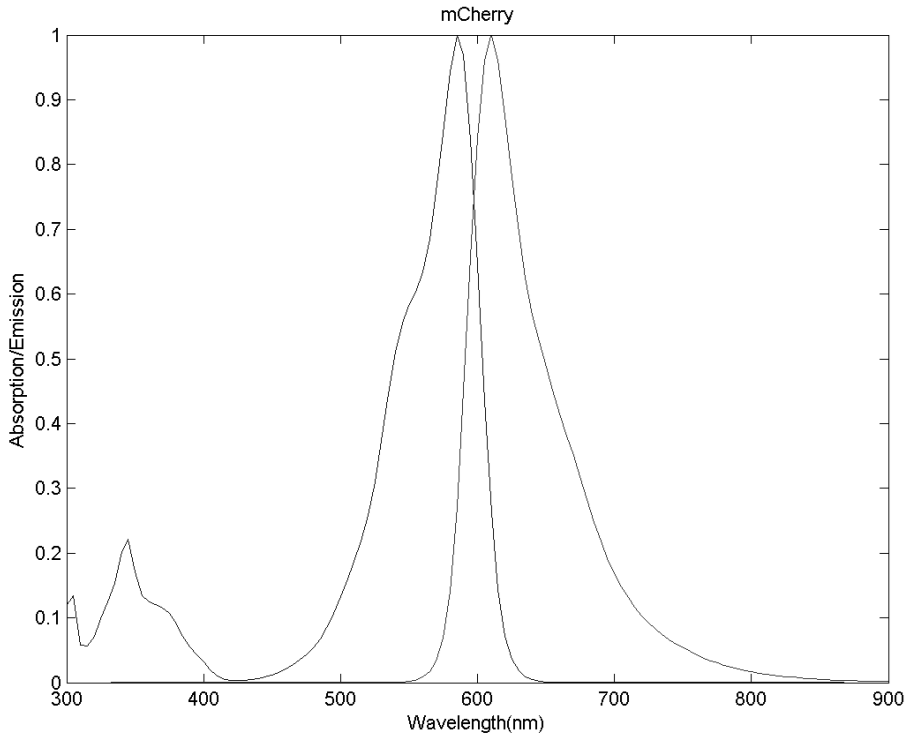

Figure 51. mCherry absorption and emission spectra

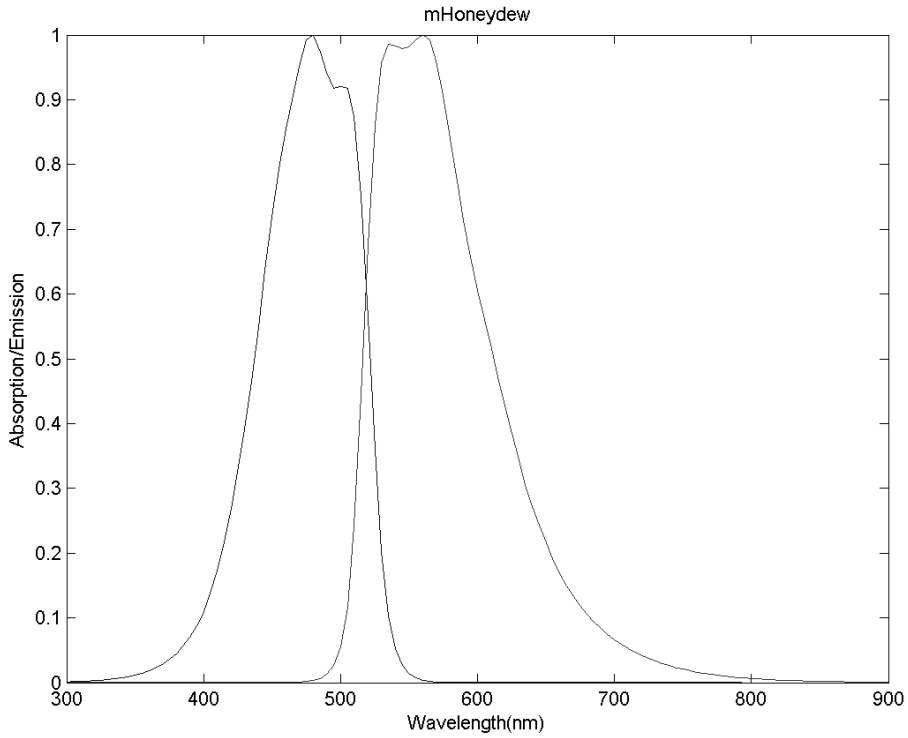

Figure 52. mHoneydew absorption and emission spectra

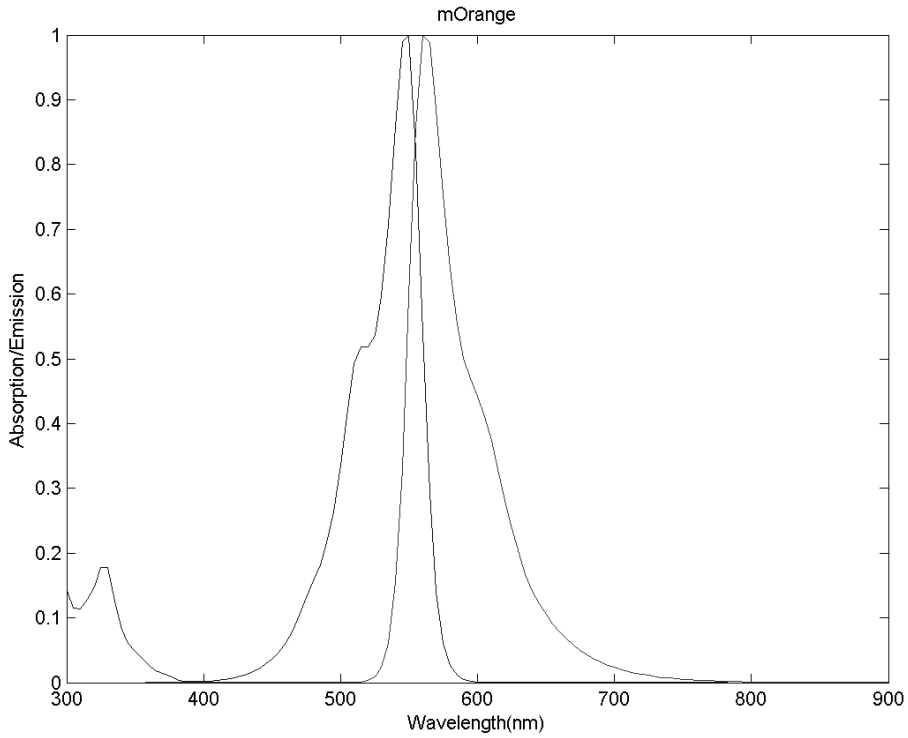

Figure 53. mOrange absorption and emission spectra

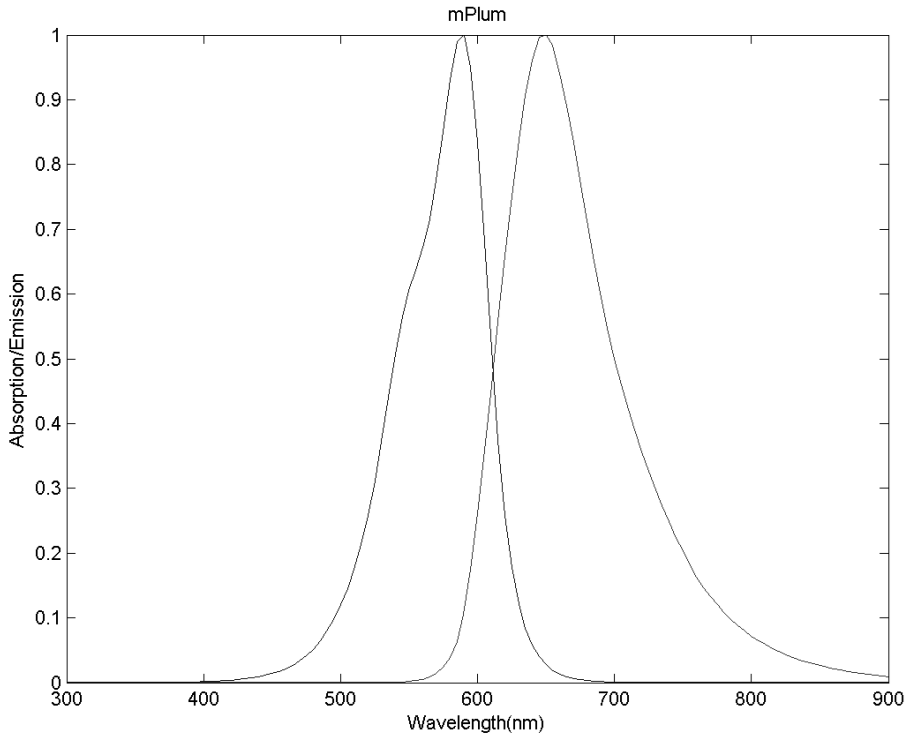

Figure 54. mPlum absorption and emission spectra

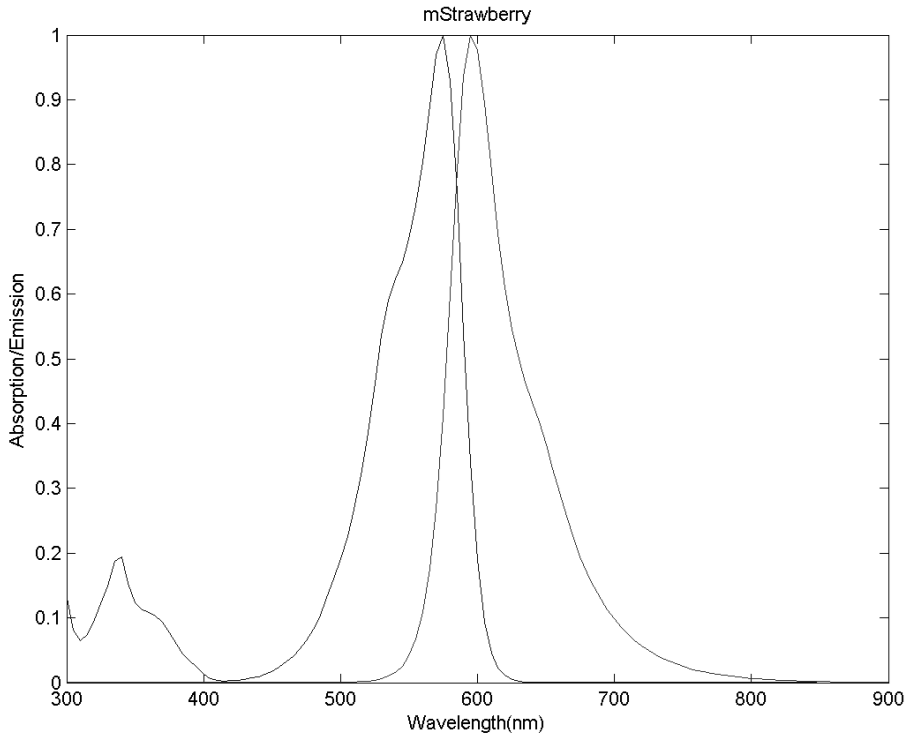

Figure 55. mStrawberry absorption and emission spectra

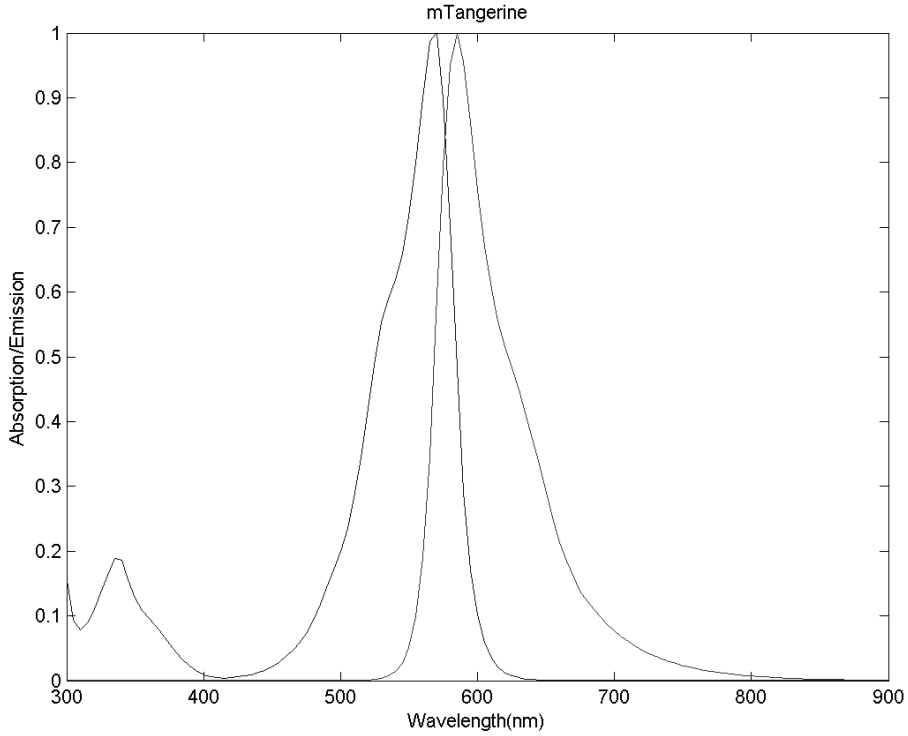

Figure 56. mTangerine absorption and emission spectra

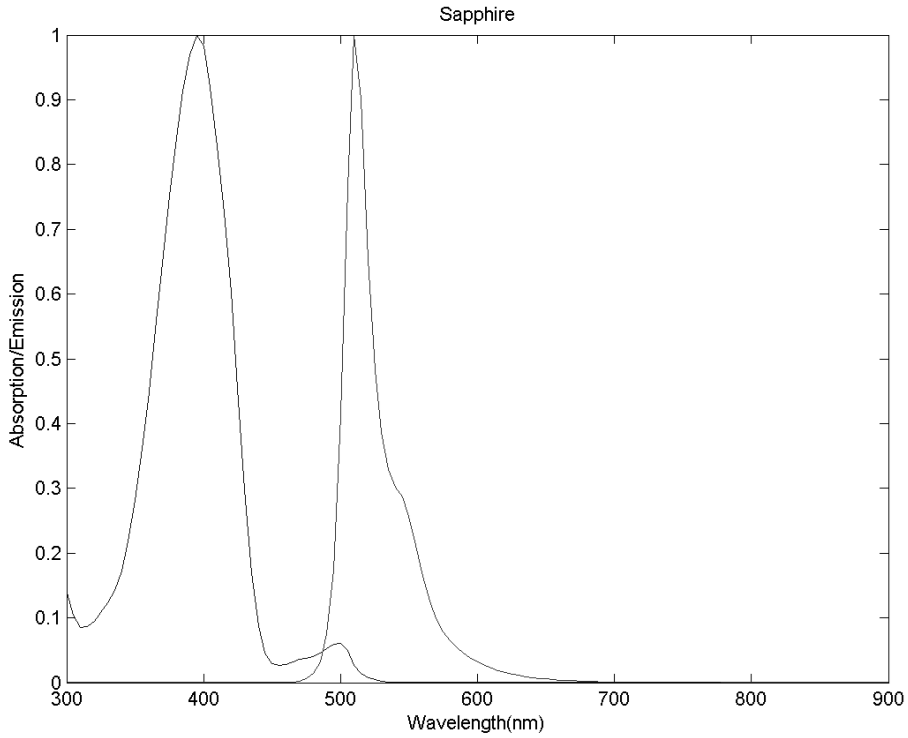

Figure 57. Sapphire absorption and emission spectra

Appendix 2. MATLAB codes

//

Single FP, two color mixing

```
% Single FP, two color mixing
clear  all
clc
tic
total = 2400;
CRI = zeros(1,total);
test = zeros(81,total);
CCT = zeros(1,total);
LER = zeros(1,total);
peak = 0;
count = 0;

mHoneydew = dlmread('mHoneydewemission.txt');
XYZ = dlmread('XYZ.txt');
Wavelength=XYZ(:,1);
lambda = mHoneydew(:,1);
for i = 1:length(Wavelength)

    for j = 1:length(lambda)

        if ((Wavelength(i)-lambda(j))<0.2 && -0.1<(Wavelength(i)-
lambda(j)))
            mHoneydewE(i,:) = mHoneydew(j,:);
        end
    end
end


BLUESTD = randi([40 40],1,1)/2.35;
BLUEMEAN = randi([465 465],1,1);

blue = (1/(BLUESTD*sqrt(2*pi)))*exp(-0.5*((Wavelength-
BLUEMEAN)/BLUESTD).^2);
blue = blue/max(blue);
blue = [Wavelength blue];


for k =1:20
    bluee(:,2) = k*blue(:,2);
    for l = 1:20
        mHoneydewEE(:,1) = mHoneydewE(:,1);
        mHoneydewEE(:,2) = l*mHoneydewE(:,2);

        for t = 0:1:6
```

```
            mHoneydewEEE(:,1) = mHoneydewEE(:,1);
            mHoneydewEEE(:,2) = circshift(mHoneydewEE(:,2),t);
            count = count +1;
            WLED(:,1) = mHoneydewE(:,1);
            WLED(:,2) = mHoneydewEEE(:,2) + bluee(:,2);
            LER(count) = 683*sum(WLED(:,2).*XYZ(:,3))/sum(WLED(:,2));

            [CRItest,photo]= myfun2(WLED);
            M(k,l,t+1) = CRItest;
            CRI(count) = CRItest;
            test(:,count) = WLED(:,2);
            CCT(count) = photo.CCT;
            if(CRItest>60)
                peak = [peak t];
            else
            end

        end
    end
end

figure(1)

plot(LER,CRI,'*')
xlabel('LER')
ylabel('CRI')
title('LER vs CRI')
ylim([50 100])
figure(2)
subplot(1,2,1)

[freq, xout] = hist(CRI,20);
bar(xout,100*freq/sum(freq))
xlim([0 100])
xlabel('CRI')
ylabel('% of samples')
title('Histogram')

[bbb,aaa] = max(CRI)

subplot(1,2,2)

plot(Wavelength,test(:,(aaa)))

xlabel('Wavelength (nm)')
ylabel('Intensity')
title('Highest CRI spectra')
WLED = [Wavelength test(:,(aaa))];
[CRItest,photo]= myfun2(WLED);
photo.x
photo.y
```

```
//////////////////////////////////////////////////////////////////

//////////////////////////////////////////////////////////////////
```

Double FP, three color mixing

```
% Double FP, three color mixing
clear  all
clc
tic
total = 121500;
CRI = zeros(1,total);
test = zeros(81,total);
CCT = zeros(1,total);
LER = zeros(1,total);


count = 0;

eGFP = dlmread('eGFPemission.txt');
mCherry = dlmread('mCherryemission.txt');
XYZ = dlmread('XYZ.txt');
Wavelength=XYZ(:,1);
lambda = eGFP(:,1);
for i = 1:length(Wavelength)

    for j = 1:length(lambda)

        if ((Wavelength(i)-lambda(j))<0.2 && -0.1<(Wavelength(i)-
lambda(j)))
            eGFPE(i,:) = eGFP(j,:);
        end
    end
end

for i = 1:length(Wavelength)
    lambda = mCherry(:,1);

    for j = 1:length(lambda)

        if ((Wavelength(i)-lambda(j))<0.2 && -0.1<(Wavelength(i)-
lambda(j)))
            mCherryE(i,:) = mCherry(j,:);
        end
    end
```

```
end
BLUESTD = randi([40 40],1,1)/2.35;
BLUEMEAN = randi([465 465],1,1);

blue = (1/(BLUESTD*sqrt(2*pi)))*exp(-0.5*((Wavelength-
BLUEMEAN)/BLUESTD).^2);
blue = blue/max(blue);
blue = [Wavelength blue];


for k =1:15
    bluee(:,2) = k*blue(:,2);
    for l = 1:15
        eGFPEE(:,1) = eGFPE(:,1);
        eGFPEE(:,2) = l*eGFPE(:,2);
        for t = 0:1:6
            eGFPEEE(:,1) = eGFPEE(:,1);
            eGFPEEE(:,2) = circshift(eGFPEE(:,2),t);
            for m = 1:15
                mCherryEE(:,1) = mCherryE(:,1);
                mCherryEE(:,2) = m*mCherryE(:,2);
                for z = 0:1:6
                    count = count +1;
                    mCherryEEE(:,1) = m*mCherryEE(:,1);
                    mCherryEEE(:,2) = circshift(mCherryEE(:,2),z);
                    WLED(:,1) = eGFPE(:,1);
                    WLED(:,2) = eGFPEEE(:,2) + mCherryEEE(:,2) +
bluee(:,2);
                    LER(count) =
683*sum(WLED(:,2).*XYZ(:,3))/sum(WLED(:,2));

                    [CRItest,photo]= myfun2(WLED);
                    CRI(count) = CRItest;
                    test(:,count) = WLED(:,2);
                    CCT(count) = photo.CCT;
                end
            end
        end
    end
end

figure(1)

plot(LER,CRI,'*')
xlabel('LER')
ylabel('CRI')
title('LER vs CRI')
ylim([50 100])
figure(2)
subplot(1,2,1)
```

```
[freq, xout] = hist(CRI,20);
bar(xout,100*freq/sum(freq))
xlim([0 100])
xlabel('CRI')
ylabel('% of samples')
title('Histogram')

[bbb,aaa] = max(CRI)

subplot(1,2,2)

plot(Wavelength,test(:,(aaa)))

xlabel('Wavelength (nm)')
ylabel('Intensity')
title('Highest CRI spectra')
WLED = [Wavelength test(:,(aaa))];
[CRItest,photo]= myfun2(WLED);
photo.x
photo.y



//////////////////////////////////////////////////////////////////


//////////////////////////////////////////////////////////////////
```

Triple FP, four color mixing

```
% Triple FP, four color mixing
tic
clear all
clc
count = 0;
total = 135000;
CRI = zeros(1,total);
test = zeros(81,total);
CCT = zeros(1,total);
LER = zeros(1,total);
peaky = 0;
peakg = 0;
peakr = 0;

eGFP = dlmread('eGFPemission.txt');
mBanana = dlmread('mBananaemission.txt');
mCherry = dlmread('mCherryemission.txt');
XYZ = dlmread('XYZ.txt');
Wavelength=XYZ(:,1);
lambda = mBanana(:,1);
for i = 1:length(Wavelength)
```

```
    for j = 1:length(lambda)

        if ((Wavelength(i)-lambda(j))<0.2 && -0.1<(Wavelength(i)-
lambda(j)))
            mBananaE(i,:) = mBanana(j,:);
        end
    end
end
lambda = eGFP(:,1);
for i = 1:length(Wavelength)

    for j = 1:length(lambda)

        if ((Wavelength(i)-lambda(j))<0.2 && -0.1<(Wavelength(i)-
lambda(j)))
            eGFPE(i,:) = eGFP(j,:);
        end
    end
end

for i = 1:length(Wavelength)
    lambda = mCherry(:,1);

    for j = 1:length(lambda)

        if ((Wavelength(i)-lambda(j))<0.2 && -0.1<(Wavelength(i)-
lambda(j)))
            mCherryE(i,:) = mCherry(j,:);
        end
    end
end
BLUESTD = randi([40 40],1,1)/2.35;
BLUEMEAN = randi([465 465],1,1);

blue = (1/(BLUESTD*sqrt(2*pi)))*exp(-0.5*((Wavelength-
BLUEMEAN)/BLUESTD).^2);
blue = blue/max(blue);
blue = [Wavelength blue];


for k =1:5
    bluee(:,2) = k*blue(:,2);
    for w =1:5
        mBananaEE(:,2) = w*mBananaE(:,2);
        mBananaEE(:,1) = mBananaE(:,1);
        for x = 0:1:6
            mBananaEEE(:,2) = circshift(mBananaEE(:,2),x);
            mBananaEEE(:,1) = mBananaEE(:,1);
            for l = 1:5
                eGFPEE(:,2) = l*eGFPE(:,2);
                eGFPEE(:,1) = eGFPE(:,1);
```

```
                for t = 0:1:6
                    eGFPEEE(:,2) = circshift(eGFPEE(:,2),t);
                    eGFPEEE(:,1) = eGFPEE(:,1);
                    for m = 1:5
                        mCherryEE(:,2) = m*mCherryE(:,2);
                        mCherryEE(:,1) = mCherryE(:,1);
                        for z = 0:1:6
                            count = count +1;
                            mCherryEEE(:,2) =
circshift(mCherryEE(:,2),z);
                            mCherryEEE(:,1) = m*mCherryEE(:,1);
                            WLED(:,1) = eGFPE(:,1);
                            WLED(:,2) = mBananaEEE(:,2) + eGFPEEE(:,2)
+ mCherryEEE(:,2) + bluee(:,2);
                            [CRItest,photo]= myfun2(WLED);
                            CRI(count) = CRItest;
                            test(:,count) = WLED(:,2);
                            LER(count) =
683*sum(WLED(:,2).*XYZ(:,3))/sum(WLED(:,2));
                            CCT(count) = photo.CCT;
                            if(CRItest>80)
                                peaky = [peaky x];
                                peakg = [peakg t];
                                peakr = [peakr z];
                            else
                            end

                        end
                    end
                end
            end
        end
    end
end
figure(1)

plot(LER,CRI,'*')
xlabel('LER')
ylabel('CRI')
title('LER vs CRI')
ylim([50 100])
figure(2)
subplot(1,2,1)

[freq, xout] = hist(CRI,20);
bar(xout,100*freq/sum(freq))
xlim([0 100])
xlabel('CRI')
ylabel('% of samples')
title('Histogram')

[bbb,aaa] = max(CRI)
```

```
subplot(1,2,2)

plot(Wavelength,test(:,(aaa)))

xlabel('Wavelength (nm)')
ylabel('Intensity')
title('Highest CRI spectra')
WLED = [Wavelength test(:,(aaa))];
[CRItest,photo]= myfun2(WLED);
photo.x
photo.y

////////////////////////////////////////////////////////////////
```

Bibliography

1. Bergh, A., et al., *The promise and challenge of solid-state lighting.* Physics today, 2001. **54**(12): p. 42-47.
2. Chien, C.-L.C., et al., *Polymer dispensing and embossing technology for the lens type LED packaging.* Journal of Micromechanics and Microengineering, 2013. **23**(6): p. 065019.
3. Irvine-Halliday, D., et al., *Solid-state lighting: the only solution for the developing world.* SPIE Newsroom, 2006. **10**(2.1200601): p. 0056.
4. Tsao, J.Y., *The US" LEDs for general illumination 2002" roadmap*. 2003, Sandia National Laboratories.
5. Yang, A. *MLS Builds Global LED Lighting Manufacturing Base to Embrace LED Golden Age*. 2014; Available from: http://www.ledinside.com/news/2014/11/mls_builds_global_led_lighting_manufacturing_base_to_embrace_led_golden_age.
6. Tsao, J.Y., *Solid-state lighting: lamps, chips, and materials for tomorrow.* IEEE Circuits and Devices Magazine, 2004. **20**(3): p. 28-37.
7. Kyle, B., *New EPA Report Shows We are Generating More E-waste But Also Recycling More.* 2013.
8. Sesini, M., *The garbage patch in the oceans: the problem and possible solutions.* Columbia University, New York, 2011.
9. Fratzl, P., J.W. Dunlop, and R. Weinkamer, *Materials Design Inspired by Nature: Function Through Inner Architecture*. 2013: Royal Society of Chemistry.
10. Hwang, S.-W., et al., *A physically transient form of silicon electronics.* Science, 2012. **337**(6102): p. 1640-1644.
11. Yin, L., et al., *Materials, designs, and operational characteristics for fully biodegradable primary batteries.* Advanced Materials, 2014. **26**(23): p. 3879-3884.
12. Jung, Y.H., et al., *High-performance green flexible electronics based on biodegradable cellulose nanofibril paper.* Nature communications, 2015. **6**.
13. Omenetto, F.G. and D.L. Kaplan, *New opportunities for an ancient material.* Science, 2010. **329**(5991): p. 528-531.
14. Fan, X. and S.-H. Yun, *The potential of optofluidic biolasers.* Nature methods, 2014. **11**(2): p. 141-147.
15. Vukusic, P. and J.R. Sambles, *Photonic structures in biology.* Nature, 2003. **424**(6950): p. 852-855.
16. Deisseroth, K., *Optogenetics.* Nature methods, 2011. **8**(1): p. 26-29.

17. Omenetto, F.G. and D.L. Kaplan, *A new route for silk.* Nature Photonics, 2008. **2**(11): p. 641-643.

18. Steckl, A.J., *DNA–a new material for photonics?* Nature Photonics, 2007. **1**(1): p. 3-5.

19. Gomez, E.F., et al., *DNA Bases Thymine and Adenine in Bio-Organic Light Emitting Diodes.* Scientific Reports, 2014. **4**.

20. Nizamoglu, S., M.C. Gather, and S.H. Yun, *All-Biomaterial Laser Using Vitamin and Biopolymers.* Advanced Materials, 2013. **25**(41): p. 5943-5947.

21. Xin, H., et al., *Escherichia coli-based biophotonic waveguides.* Nano letters, 2013. **13**(7): p. 3408-3413.

22. Jain, A., A.H. Yang, and D. Erickson, *Gel-based optical waveguides with live cell encapsulation and integrated microfluidics.* Optics letters, 2012. **37**(9): p. 1472-1474.

23. Large, M., *Optical biomimetics: materials and applications*. 2012: Elsevier.

24. Murr, L.E., *Biomimetics and Biologically Inspired Materials*, in *Handbook of Materials Structures, Properties, Processing and Performance*. 2014, Springer. p. 1-28.

25. Schubert, E.F., T. Gessmann, and J.K. Kim, *Light emitting diodes*. 2005: Wiley Online Library.

26. Hussain, S.A., *An introduction to fluorescence resonance energy transfer (FRET).* arXiv preprint arXiv:0908.1815, 2009.

27. !!! INVALID CITATION !!!

28. Kasap, S.O., *Optoelectronics & Photonics: Principles & Practices: International Edition*. 2013: Pearson Higher Ed.

29. Yamada, M., et al., *A methodological study of the best solution for generating white light using nitride-based light-emitting diodes.* IEICE transactions on electronics, 2005. **88**(9): p. 1860-1871.

30. Damilano, B., et al., *Monolithic white light emitting diodes using a (Ga, In) N/GaN multiple quantum well light converter.* Applied Physics Letters, 2008. **93**(10): p. 101117.

31. Pimputkar, S., et al., *Prospects for LED lighting.* Nature Photonics, 2009. **3**(4): p. 180-182.

32. Swanson, S.A., et al., *Stable and efficient fluorescent red and green dyes for external and internal conversion of blue OLED emission.* Chemistry of materials, 2003. **15**(12): p. 2305-2312.

33. Tasch, S., et al., *Efficient red-and orange-light-emitting diodes realized by excitation energy transfer from blue-light-emitting conjugated polymers.* Physical Review B, 1997. **56**(8): p. 4479.

34. Chalfie, M. and S.R. Kain, *Green fluorescent protein: properties, applications and protocols*. Vol. 47. 2005: John Wiley & Sons.

35. Chudakov, D.M., et al., *Fluorescent proteins and their applications in imaging living cells and tissues.* Physiological reviews, 2010. **90**(3): p. 1103-1163.

36. Shaner, N.C., G.H. Patterson, and M.W. Davidson, *Advances in fluorescent protein technology.* Journal of cell science, 2007. **120**(24): p. 4247-4260.

37. Phillips, J.M., et al., *Research challenges to ultra-efficient inorganic solid-state lighting.* Laser & Photonics Reviews, 2007. **1**(4): p. 307-333.

38. Humphreys, C.J., *Solid-State Lighting.* MRS Bulletin, 2008. **33**(04): p. 459-470.

39. Crawford, M.H., et al., *Solid-State Lighting: Toward Smart and Ultraefficient Materials, Devices, Lamps, and Systems*, in *Photonics*. 2015, John Wiley & Sons, Inc. p. 1-56.

40. *The new oil?* Nat Photon, 2011. **5**(1): p. 1-1.

41. Demir, H.V., et al., *Quantum dot integrated LEDs using photonic and excitonic color conversion.* Nano Today, 2011. **6**(6): p. 632-647.

42. Kirchner, C., et al., *Cytotoxicity of Colloidal CdSe and CdSe/ZnS Nanoparticles.* Nano Letters, 2005. **5**(2): p. 331-338.

43. van Embden, J., A.S.R. Chesman, and J.J. Jasieniak, *The Heat-Up Synthesis of Colloidal Nanocrystals.* Chemistry of Materials, 2015. **27**(7): p. 2246-2285.

44. Peng, X., et al., *Shape control of CdSe nanocrystals.* Nature, 2000. **404**(6773): p. 59-61.

45. Yen, B.K., et al., *A Continuous-Flow Microcapillary Reactor for the Preparation of a Size Series of CdSe Nanocrystals.* Advanced Materials, 2003. **15**(21): p. 1858-1862.

46. Yang, S.J., et al., *Realization of InP/ZnS quantum dots for green, amber and red down-converted LEDs and their color-tunable, four-package white LEDs.* Journal of Materials Chemistry C, 2015. **3**(15): p. 3582-3591.

47. Oberdörster, G., E. Oberdörster, and J. Oberdörster, *Nanotoxicology: an emerging discipline evolving from studies of ultrafine particles.* Environmental health perspectives, 2005: p. 823-839.

48. Weber, M.D., et al., *Bioinspired Hybrid White Light-Emitting Diodes.* Advanced Materials, 2015. **27**(37): p. 5493-5498.

49. Gather, M.C. and S.H. Yun, *Bio-optimized energy transfer in densely packed fluorescent protein enables near-maximal luminescence and solid-state lasers.* Nat Commun, 2014. **5**.

50. Giepmans, B.N., et al., *The fluorescent toolbox for assessing protein location and function.* Science, 2006. **312**(5771): p. 217-224.

51. Day, R.N. and M.W. Davidson, *The fluorescent protein palette: tools for cellular imaging.* Chemical Society Reviews, 2009. **38**(10): p. 2887-2921.

52. Rockwood, D.N., et al., *Materials fabrication from Bombyx mori silk fibroin.* Nature protocols, 2011. **6**(10): p. 1612-1631.

53. Oh, J.H., et al., *Analysis of wide color gamut of green/red bilayered freestanding phosphor film-capped white LEDs for LCD backlight.* Optics express, 2015. **23**(15): p. A791-A804.

54. Gather, M.C. and S.H. Yun, *Bio-optimized energy transfer in densely packed fluorescent protein enables near-maximal luminescence and solid-state lasers.* Nature Communications, 2014. **5**.

55. Stryer, L., *Fluorescence energy transfer as a spectroscopic ruler.* Annual review of biochemistry, 1978. **47**(1): p. 819-846.

56. Akrap, N., T. Seidel, and B.G. Barisas, *Förster distances for fluorescence resonant energy transfer between mCherry and other visible fluorescent proteins.* Analytical biochemistry, 2010. **402**(1): p. 105-106.

57. Lin, Y., et al., *The effect of spectrum on visual field in road lighting.* Building and environment, 2004. **39**(4): p. 433-439.

58. Gather, M.C. and S.H. Yun, *Single-cell biological lasers.* Nat Photon, 2011. **5**(7): p. 406-410.

59. Gather, M.C. and S.H. Yun, *Lasing from Escherichia coli bacteria genetically programmed to express green fluorescent protein.* Optics letters, 2011. **36**(16): p. 3299-3301.

60. Amsterdam, A., S. Lin, and N. Hopkins, *The Aequorea victoria green fluorescent protein can be used as a reporter in live zebrafish embryos.* Developmental biology, 1995. **171**(1): p. 123-129.

61. Okabe, M., et al., *Green mice'as a source of ubiquitous green cells.* FEBS letters, 1997. **407**(3): p. 313-319.

62. Klaine, S.J., et al., *Nanomaterials in the environment: behavior, fate, bioavailability, and effects.* Environmental Toxicology and Chemistry, 2008. **27**(9): p. 1825-1851.

63. *Table of Fluorescent Proteins - NIC@UCSF*. 17/10/2013 [cited 2015 27/10]; Available from: http://nic.ucsf.edu/dokuwiki/doku.php?id=fluorescent_proteins.

64. Steigerwald, M.L. and L.E. Brus, *Synthesis, stabilization, and electronic structure of quantum semiconductor nanoclusters.* Annual Review of Materials Science, 1989. **19**(1): p. 471-495.

65. Dabbousi, B., et al., *(CdSe) ZnS core-shell quantum dots: synthesis and characterization of a size series of highly luminescent nanocrystallites.* The Journal of Physical Chemistry B, 1997. **101**(46): p. 9463-9475.

66. Shaner, N.C., P.A. Steinbach, and R.Y. Tsien, *A guide to choosing fluorescent proteins.* Nature methods, 2005. **2**(12): p. 905-909.

67. Eberspacher, C. and V.M. Fthenakis. *Disposal and recycling of end-of-life PV modules*. in *Photovoltaic Specialists Conference, 1997., Conference Record of the Twenty-Sixth IEEE*. 1997. IEEE.

68. Irimia-Vladu, M., *"Green" electronics: biodegradable and biocompatible materials and devices for sustainable future.* Chemical Society Reviews, 2014. **43**(2): p. 588-610.

69. Hoffman, A.S., *Hydrogels for biomedical applications.* Advanced drug delivery reviews, 2012. **64**: p. 18-23.

70. Choi, M., et al., *Light-guiding hydrogels for cell-based sensing and optogenetic synthesis in vivo.* Nature photonics, 2013. **7**(12): p. 987-994.

71. Jones, L., N. Macdougall, and L.G. Sorbara, *Asymptomatic corneal staining associated with the use of balafilcon silicone-hydrogel contact lenses disinfected with a polyaminopropyl biguanide-preserved care regimen.* Optometry & Vision Science, 2002. **79**(12): p. 753-761.

72. Brennan, N.A., et al., *A 1-year prospective clinical trial of balafilcon a (PureVision) silicone-hydrogel contact lenses used on a 30-day continuous wear schedule.* Ophthalmology, 2002. **109**(6): p. 1172-1177.

73. Stapleton, F., et al., *Silicone hydrogel contact lenses and the ocular surface.* The ocular surface, 2006. **4**(1): p. 24-43.

74. Keay, L., et al., *Microcyst response to high Dk/t silicone hydrogel contact lenses.* Optometry & Vision Science, 2000. **77**(11): p. 582-585.

75. Nicolson, P.C. and J. Vogt, *Soft contact lens polymers: an evolution.* Biomaterials, 2001. **22**(24): p. 3273-3283.

76. Min, B.-M., et al., *Electrospinning of silk fibroin nanofibers and its effect on the adhesion and spreading of normal human keratinocytes and fibroblasts in vitro.* Biomaterials, 2004. **25**(7): p. 1289-1297.

77. Motta, A., et al., *Fibroin hydrogels for biomedical applications: preparation, characterization and in vitro cell culture studies.* Journal of biomaterials science, Polymer edition, 2004. **15**(7): p. 851-864.

78. Murphy, A.R. and D.L. Kaplan, *Biomedical applications of chemically-modified silk fibroin.* Journal of materials chemistry, 2009. **19**(36): p. 6443-6450.

79. Partlow, B.P., et al., *Highly tunable elastomeric silk biomaterials.* Advanced functional materials, 2014. **24**(29): p. 4615-4624.

80. Mitropoulos, A.N., et al., *Transparent, nanostructured silk fibroin hydrogels with tunable mechanical properties.* ACS Biomaterials Science & Engineering, 2015. **1**(10): p. 964-970.

81. Part, G.T., *Silk Functionalization: Developing the Next Generation of High Performance Fibers.*

82. Applegate, M.B., et al., *Laser-based three-dimensional multiscale micropatterning of biocompatible hydrogels for customized tissue engineering scaffolds.* Proceedings of the National Academy of Sciences, 2015. **112**(39): p. 12052-12057.

83. Venyaminov, S.Y. and F.G. Prendergast, *Water (H 2 O and D 2 O) molar absorptivity in the 1000–4000 cm− 1 range and quantitative infrared spectroscopy of aqueous solutions.* Analytical biochemistry, 1997. **248**(2): p. 234-245.

84. Peppas, N.A., et al., *Hydrogels in biology and medicine: from molecular principles to bionanotechnology.* Advanced Materials, 2006. **18**(11): p. 1345-1360.

85. Yeh, J., et al., *Micromolding of shape-controlled, harvestable cell-laden hydrogels.* Biomaterials, 2006. **27**(31): p. 5391-5398.

86. Dong, L., et al., *Adaptive liquid microlenses activated by stimuli-responsive hydrogels.* Nature, 2006. **442**(7102): p. 551-554.

87. Camras, M.D., et al., *Light emitting diodes with improved light extraction efficiency*. 2006, Google Patents.

88. Galassi, G., et al., *In vitro reconstructed dermis implanted in human wounds: degradation studies of the HA-based supporting scaffold.* Biomaterials, 2000. **21**(21): p. 2183-2191.

89. Peyman, G.A., J.E. Koziol, and H. Yasuda, *Soft corneal contact lens with tightly cross-linked polymer coating and method of making same*. 1982, Google Patents.